INFORMATION TO USERS

This manuscript has been reproduced from the microfilm master. UMI films the text directly from the original or copy submitted. Thus, some thesis and dissertation copies are in typewriter face, while others may be from any type of computer printer.

The quality of this reproduction is dependent upon the quality of the copy submitted. Broken or indistinct print, colored or poor quality illustrations and photographs, print bleedthrough, substandard margins, and improper alignment can adversely affect reproduction.

In the unlikely event that the author did not send UMI a complete manuscript and there are missing pages, these will be noted. Also, if unauthorized copyright material had to be removed, a note will indicate the deletion.

Oversize materials (e.g., maps, drawings, charts) are reproduced by sectioning the original, beginning at the upper left-hand corner and continuing from left to right in equal sections with small overlaps.

Photographs included in the original manuscript have been reproduced xerographically in this copy. Higher quality 6" x 9" black and white photographic prints are available for any photographs or illustrations appearing in this copy for an additional charge. Contact UMI directly to order.

ProQuest Information and Learning
300 North Zeeb Road, Ann Arbor, MI 48106-1346 USA
800-521-0600

UMI®

Reproduced with permission of the copyright owner. Further reproduction prohibited without permission.

DISSERTATION

A THEORY OF THE MESOSCALE ORGANIZATION OF MOIST CONVECTION AND THE ASSOCIATED VERTICAL MOMENTUM TRANSPORT

Submitted by
Anning Cheng
Department of Atmospheric Science

In partial fulfillment of the requirements
for the Degree of Doctor of Philosophy
Colorado State University
Fort Collins, Colorado
Fall 2001

ProQuest Information and Learning Company
300 North Zeeb Road
P.O. Box 1346
Ann Arbor, MI 48106-1346

COLORADO STATE UNIVERSITY

AUGUST 6, 2001

WE HEREBY RECOMMEND THAT THE DISSERTATION PREPARED UNDER OUR SUPERVISION BY ANNING CHENG ENTITLED A THEORY OF THE MESOSCALE ORGANIZATION OF MOIST CONVECTION AND THE ASSOCIATED VERTICAL MOMENTUM TRANSPORT BE ACCEPTED AS FULFILLING IN PART REQUIREMENTS FOR THE DEGREE OF DOCTOR OF PHILOSOPHY.

Committee on Graduate Work

Richard H. Johnson

Wayne Schubert

Adviser

Department Head

ABSTRACT OF DISSERTATION

A THEORY OF THE MESOSCALE ORGANIZATION OF MOIST CONVECTION AND THE ASSOCIATED VERTICAL MOMENTUM TRANSPORT

A parameterization of cumulus momentum transport is proposed. An important feature of the parameterization is the inclusion of the perturbation pressure-gradient force induced by interactions between the updraft and the environmental wind. The orientation, aspect ratio, phase speed and size of the organized convection are determined. These quantities depend on the vertical wind-shear and the stratification.

GATE, ARM, EMEX, SCSMEX, and TOGA COARE data are used to test the theory. Results show that: 1) the predicted orientation, aspect ratio, and phase speed of organized convection agree well with the observations. 2) the vertical momentum transport is sensitive to the orientation of the cumulus clouds; 3) the momentum transport due to the perturbation pressure-gradient force tends to be upgradient and to cancel with the vertical momentum advection and detrainment effects. 4) the shear term produces positive convective kinetic energy (CKE), or negative CKE, depending on the vertical wind-shear and the velocity difference between the clouds and the environment; and 5) the CKE produced by shear accounts for about 1% of that by buoyancy, so its influence is very small in the cases studied here.

Anning Cheng
Atmospheric Science Department
Colorado State University
Fort Collins, CO 80523
Fall 2001

ACKNOWLEDGMENTS

I would like to thank my advisor, Professor David A. Randall, for his guidance, understanding and inspiration during my Ph. D. work. He enlightened me not only in science, but also in improving my writing skill. The "300-level" technical writing course will be helpful for my future career. Thanks also go to Professors Wayne H. Schubert, Richard H. Johnson and Steven H. Strauss, my Committee members, for their constructive suggestions and their valuable time.

Thanks also go to Douglas Cripe and Don Dazlich for their help on using CSU SCM. I am grateful to Kuanman Xu, Xin Lin, and Randall's Rabbits for their help. Cindy Carrick and Kelley Wittmeyer have been of great help. I also thank Paul Hein, Walt Petersen, and Professor Steven Rutledge provide CSU-MIT radar image for TOGA COARE.

I would like to give my thanks to my wife Shengtao Dong. Her continuous support and encouragement are so valuable for me. I also thank my friends and other family members.

This study has been supported by National Science Foundation under grant ATM-9812384 and by the U.S. Department of Energy's ARM Program under grant DE-FG03-95ER61968.

TABLE OF CONTENTS

Chapter I: Introduction

I-A: Background

An important effect of cumulus convection is the vertical redistribution of momentum. The momentum residual caused by the organized cumulus clouds is typically about 1 $\mathrm{ms}^{-1}\mathrm{day}^{-1}$ (e. g. Tollerud and Esbensen, 1983; Wu and Yanai, 1994). Fig. 1 shows the effects of the cumulus momentum redistribution. All lines in the figure are numbered. The momentum redistribution will influence the convective kinetic energy (CKE; line1), which will cause the change of entrainment, detrainment rate and mass flux (line 2). The entrainment, detrainment rate and mass flux will determine the intensity of the updraft and downdraft (line 3). The updraft tilting angle is determined by its three momentum components. In order to calculate these components, the momentum transport by convective clouds must be considered (line 4). The tilting of the updraft interacts with the rainwater loading and updraft vertical velocity (line 5), which in turn influence the convective updraft and downdraft (line 6).

The trajectories of the parcels inside convective cloud tend to be along the tilting updraft and to be influenced by the convective momentum transport (line 7). The trajectories of the parcels can also be used to check for the conditional symmetric instability (CSI; Emanuel, 1983; line 8). If most of the parcels inside a mesoscale updraft move along a slantwise surface of constant angular momentum, part of the updraft kinetic energy can be converted from large-scale kinetic energy. As a mesoscale system, the CSI

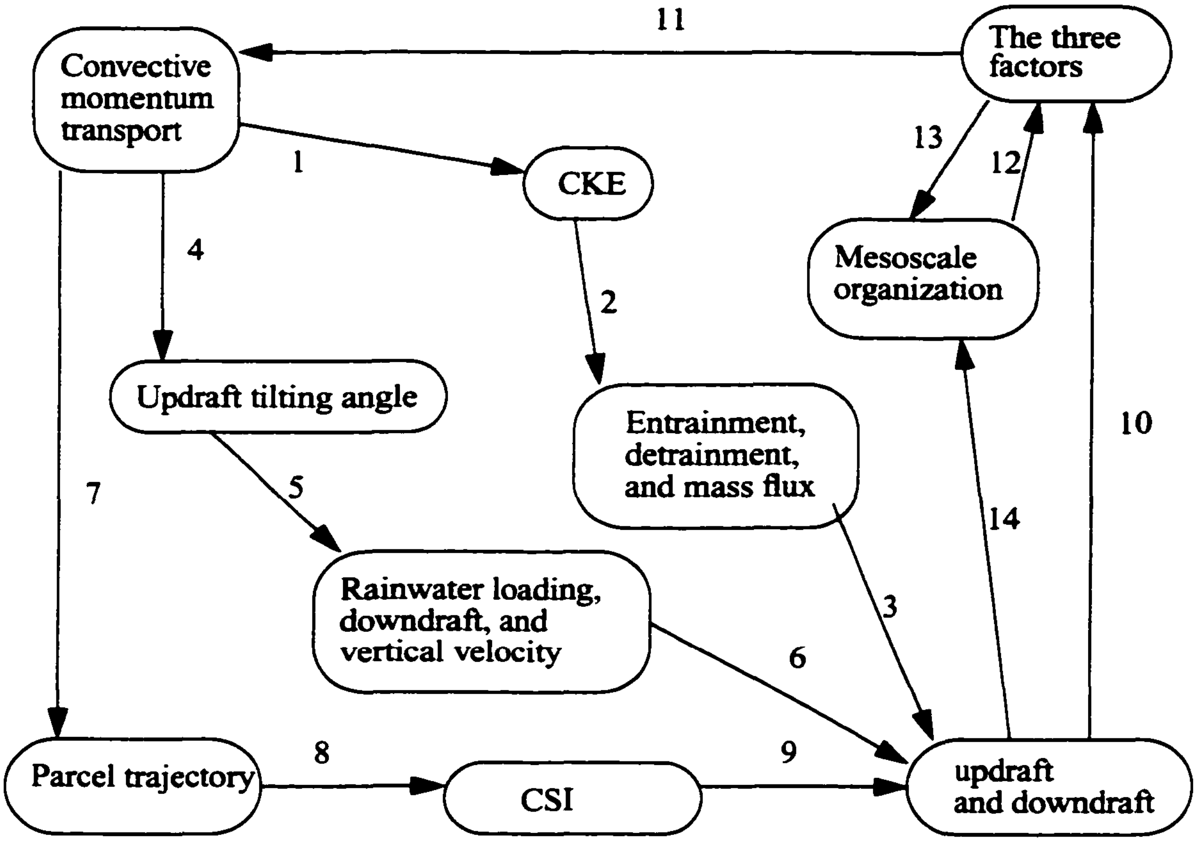

Figure 1: Effects of convective momentum transport by cumulus clouds.

will influence the intensity and the location of the convective updrafts and downdrafts (line 9; Tomas and Webster, 1997).

There are three factors influencing the vertical momentum transport by cumulus clouds (line 11): the subsidence of the environmental air associated with the cumulus mass flux, the detrainment of momentum from clouds, and the convective-scale horizontal pressure-gradient force. There is no doubt that these three factors are determined by the updraft, downdraft and large-scale fields (line 10; explained in Chapter II). The major effect of the first two factors is a kind of mixing, and downgradient vertical momentum transport is caused by these two effects in many cases. The third factor, the perturbation pressure-gradient force, is very important for causing systematic upgradient momentum transport in convective clouds. It is mainly produced by the interactions between the updraft and the vertical wind-shear. Usually a high pressure is produced upshear, and a low pressure down shear. The effects of the perturbation pressure-gradient force tend to cancel the effects of the first two factors. The perturbation pressure-gradient force strongly depends on the spatial organization of the cumulus clouds (line 12). For example Linear Mesoscale Convective Systems (MCSs), in which the clouds are organized along a line (i. e., a squall line), and nonlinear MCSs, in which the clouds are organized as a quasi-circular mass, produce totally different vertical momentum transports. This is because linear MCSs produce a large perturbation pressure-gradient force in the line-normal direction. In this direction, there is a large "contact area" (defined as the area of a mesoscale system confronting the mean wind; see Fig. 2) between the vertical wind-shear and the updraft. However, in the line-parallel direction for MCSs, and in every direction for nonlinear MCSs, the contact area between the vertical wind-shear and the updraft is small. The larger the contact area, the more influence the perturbation pressure-gradient force has on the convective clouds. The organization of a mesoscale system is also influenced by the momentum detrainment and vertical advection (line 13) and by heat and moist detrainment and advection (line 14).

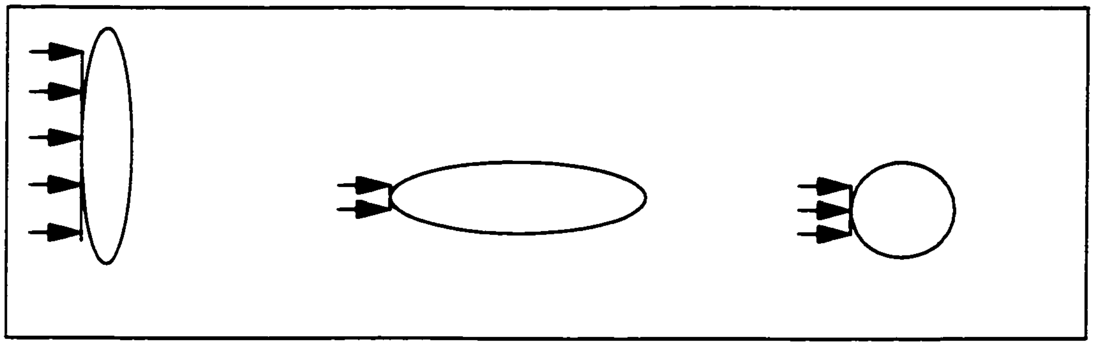

Figure 2: The cross section of a contact area in a horizontal plane. The line normal direction has a large contact area.

The importance of organized cumulus clouds for momentum transport has been studied since the 1970s. Asai (1970) found that the air motion in longitudinal rolls is three-dimensional and results in a downgradient flux of horizontal momentum, and that the air motion in transverse rolls results in upgradient horizontal momentum transport. This influences the energy conversion between the basic flow and the perturbation. Using a simple two dimensional model, Moncrieff and Green (1972) showed that steady, buoyant overturning increases the vertical wind-shear. Stevens (1979) found large momentum-budget residuals in his analysis of an averaged easterly wave during GATE (the Global Atmospheric Research Program's Atlantic Tropical Experiment) Phase III. He concluded that cumulus momentum transport must be parameterized properly in order to simulate realistic large-scale waves. In this period, researchers found both downgradient and upgradient momentum transports by organized cumulus clouds, and they realized that the structure of the organized cumulus clouds is important for the momentum transport. Very simple models were used.

In the 1980s, more sophisticated models and additional observational data were used to explore the mystery of the momentum transport by cumulus clouds. The three factors influencing the vertical momentum transport, as mentioned above, were identified and emphasized. Tollerud and Esbensen (1983) and Sui and Yanai (1986) found a distinct residual dipole pattern in the vorticity budget of the upper troposphere above deep convection using GATE phase III data. Fig. 3 shows the dipole structure for the vorticity budget residual and local vorticity change with time. The depth of this couplet is about 2 km. The negative relative vorticity lies to the south of the cumulus cloud area, while the positive relative vorticity to the north. Tollerud and Esbensen's (1983) vorticity budget analysis shows that the couplets are produced by cumulonimbi or mesoscale systems. Sui and Yanai (1986) found that two factors: vertical advection effects and the detrainment effects, can explain the major features of the observed vorticity budget. Their analysis is reasonable because these two effects of the cumulus clouds overwhelm the perturbation pressure-gradient force for nonlinear MCSs. Using numerical cloud ensemble models, Soong and Tao (1984) and Tao and Soong (1986) found that the generation of horizontal momentum by the pressure-gradient force can make a large difference in the vertical momentum transport in the rain-band-normal direction.

In this period, scientists had a good understanding of the perturbation pressure-gradient force. Rotunno and Klemp (1982) argued that the perturbation pressure-gradient force produced by the interaction of the mean shear with the updraft is very important for understanding the observed cyclonically rotating, right-moving storms. Hane and Ray (1985) analyzed the pressure and buoyancy field from Doppler Radar data in a tornadic

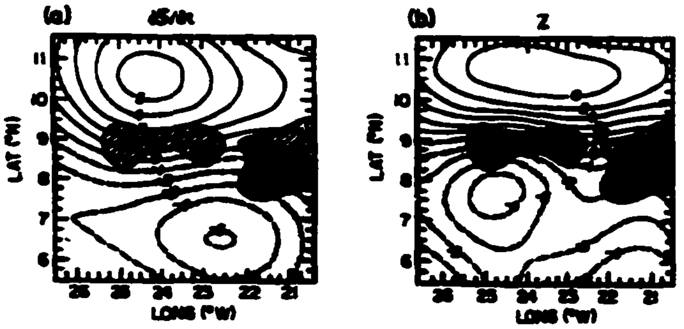

Figure 3: Composite fields of (a) local vorticity change and (b) the vorticity budget residual at 227 mb for easterly wave. Hatched regions are composite cloud cover at 300mb over 30% (Tollerud and Esbensen 1983).

thunderstorm. They found a high-low couplet across the updraft with the maximum pressure-gradient oriented along the environmental shear vector. The strong low-level vertical vorticity produced a minimum pressure at low-levels during the tornadic stage. The vorticity, vertical motion and pressure relationships in the low-level mesoscale system tend to agree pretty well. Using Server Environmental Storms and Mesoscale Experiment (SESAME) dual-Doppler data, Lin et al. (1986) found that the pressure perturbation is closely related to the structure of updraft and downdraft. High pressure forms on the upshear side of the updraft, and low pressure forms on the downshear side. LeMone et al. (1988) found that the perturbation pressure oscillation can be well predicted by assuming a sinusoidal function in the corresponding terms in the pressure diagnostic equation. The amplitude of the pressure oscillation is related to the characteristics of the vertical velocity field and the vertical wind-shear. Jorgensen et al. (1991) found that the perturbation pressure fields are consistent with the tilt of the updraft, the buoyancy distribution, and the interactions of the updraft with the vertical wind-shear. All of these works show the importance of the interactions between updraft and the environmental wind in producing the horizontal perturbation pressure-gradient force. The vertical perturbation pressure-gradient force is related to the buoyancy and the vertical velocity of the updraft.

In the 1990s, scientists gained an even better understanding of the problem. The orientation of organized cumulus clouds was taken into account. LeMone and Jorgensen (1991) reported that, for the cases they studied, the line-normal momentum transport was downgradient in the lower troposphere and upgradient in the upper troposphere. Gallus and Johnson (1992) found that horizontal momentum is not conserved inside convective updrafts. They suggested that upgradient momentum transport is associated with convective-scale pressure-gradient effects. Wu and Yanai (1994) found from AVE-SESAME (Atmospheric Variability Experiment -- Severe Environmental Storms and Mesoscale Experiment) and OK PRE-STORM (Oklahoma-Kansas Preliminary Regional Experiment for STORM-Central) data and numerical simulations that the vertical momentum transport associated with nonlinear MCSs, which they called mesoscale convective complexes[1] (MCCs), is downgradient in the upper layer. Vertical transport of the momentum component normal to a squall line is upgradient, and the transport of the component parallel to the line is downgradient in the upper layer. Fig. 4 shows vertical profiles for a squall line that occurred on10 May 1979. For the line-parallel component, the momentum residual budget decreases the upper level wind and increases the lower level wind, so the vertical transport of the horizontal momentum in line parallel direction is downgradient; for the line-perpendicular direction, the residual increases the upper level

---

[1] Johnson and Hamilton (1988) pointed out that some MCCs have linear structure.

wind and decreases the middle-level wind, so the vertical transport of the horizontal momentum in line perpendicular direction is upgradient.

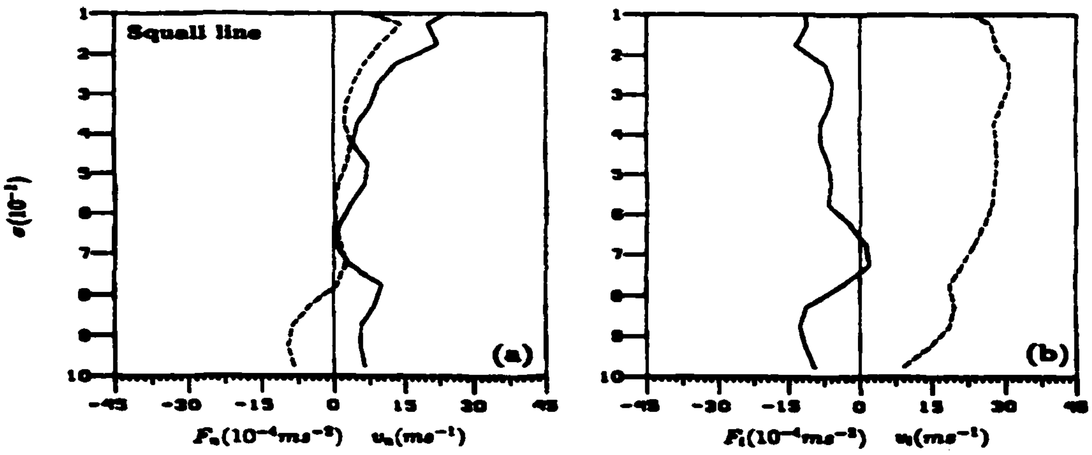

Figure 4: Vertical profile of (a) line-normal and (b) line-parallel components of observed momentum budget residual (solid) and horizontal wind (dash) at 0600 UTC 10 May during SESAME (Wu and Yanai 1994).

In the 2000s, due to the availability of data from observations, long-term and objective analysis are being used to determine the effects of the cumulus momentum transport. Studies in this period are not limited to a few individual cases. For example, Carr and Bretherton (2001) used the Tropical Ocean Global Atmosphere Coulped Ocean-Atmosphere Response Experiment (TOGA COARE) Intensive Flux Array (IFA) reanalyses data to calculate the momentum budget residual for a long period of time and for a large area. They found that the zonal residual is significant below 850 mb in all regions they analyzed. They argued that this is caused by shallow convection. In the rest of the troposphere, they found a slightly downgradient transport of zonal momentum. Using the same data sets, Tung and Yanai (2001) found that the time series of convective momentum transport (CMT) show multi-scale temporal behavior. The power spectra of CMT residual exhibit peaks near 10, 4-5 and 2 days, and at the diurnal period. They argued that the Madden-Julian Oscillation (MJO) and other disturbances produce CMT. They also show that the momentum transport is downgradient on average. However, there are some disadvantages for these long term analyses. The sparser observations may cause a problem. If they are averaged in a large area, the effects of the CMT may be excessively smoothed. The systematic upgradient momentum transport by linear MCSs cannot be seen if we do not distinguish between nonlinear MCSs and linear MCSs in long term analyses.

I-B: Convective momentum transport parameterizations

During this period, some convective momentum transport parameterizations including the perturbation pressure-gradient force were developed.

Many attempts have been made to parameterize the dynamical effects of cumulus convection in terms of large-scale variables. However, the convective-scale horizontal pressure-gradient force was ignored in most studies before 1990. Detrainment and environmental subsidence can partially explain the observed momentum budget residuals, but large systematic differences occur when the vertical shear is strong (Sui et al. 1989).

Moncrieff's (1992) "archetypal" two-dimensional model is based on a set of conservation principles and integral constraints. Three configurations (see Fig. 5) are considered: the jump updraft, an overturning updraft (downdraft) in the rear of the system and an overturning updraft (currents in anvil) in the front. This is a very beautiful model of the vertical transport of horizontal momentum. It has the potential to catch the downdraft and the anvil easily. Some studies have shown that the momentum transport predicted by this idealized model is consistent with observations for low values of the Richardson number[2] and in the absence of extensive stratiform clouds (Moncrieff 1992, and LeMone and Moncrieff 1994). Application of the model requires a method to activate the scheme, the scale of the grid, the line orientation, the line speed, the line-parallel momentum transport, the depth of the cloud, the height of the jump updraft, and the height of the rear overturning current. Most of these parameters are not available in general circulation models (GCMs).

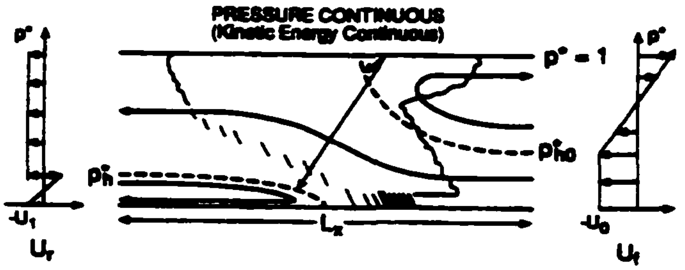

Figure 5: Schematic flow for Moncrieff's 1992 2-D model. The asterisk denotes a normalization. $u^* = u/U_0$. $p^* = (p_{sfc} - p)/(p_{sfc} - p_{top})$. U_f^* and U_r^* are the line-relative wind speeds to the front and rear of the line, respectively. p^*_{h0} is the depth of the jump updraft. p^*_h is the depth of the downdraft (called rear overturning current by Moncrieff) (from LeMone and Moncrieff 1993).

Zhang and Cho (1991a, 1991b) and Zhang and McFarlane (1995) developed a parameterization of convective momentum transport including the effects of the

---

[2] Defined as the ratio of the Convective Available Potential Energy (CAPE) to the kinetic energy associated with the shear.

perturbation pressure-gradient field. They assumed a circular structure for the cumulus clouds, so they did not distinguish between the nonlinear MCS case and the linear MCS case, and the orientation of the organized convection was not considered. In order to calculate the cloud-scale pressure-gradient force, they also assumed a couplet structure for the vertical vorticity. This couplet structure is obvious in the upper levels for the nonlinear MCSs, but not necessary at every level. Their study accounts for the effects of down-gradient convective momentum transport. Because the vertical transport of horizontal momentum by squall lines is not included in this scheme, the systemic upgradient momentum transport in the line-perpendicular direction cannot be simulated. We can say that this scheme will overestimate the down-gradient momentum transport.

Wu and Yanai (1994) developed a parameterization that includes the effects of the convective-scale pressure-gradient force acting on the updraft. Their approach has a clear physical interpretation and captures the main characteristics of the perturbation pressure-gradient force in terms of the vertical wind-shear, the cloud mass flux, and the orientation of the organized convection. Both up-gradient and down-gradient vertical momentum transports can be explained with their scheme. Fig. 6 shows that the observed momentum residual and the simulated residual from this parameterization without the convective-scale horizontal pressure-gradient force. It reveals that the there are large differences between the simulation and observation in the upper levels, for both the line-parallel and line-perpendicular components. When the convective-scale horizontal pressure-gradient force is included (Fig. 7), the differences are much smaller. Though this scheme gives good results, it cannot determine the orientation and aspect ratio of the organized convection, so it is not closed.

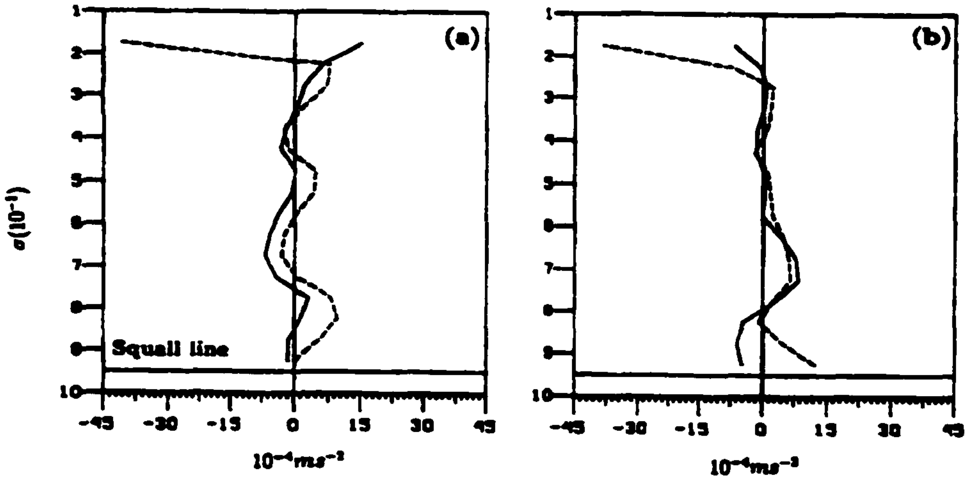

Figure 6: Vertical profiles of (a) line-normal and (b) line-parallel components of observed momentum budget residual (solid) and cumulus-induced acceleration simulated using the cloud momentum model without the convective-scale horizontal pressure-gradient force (dashed) at 2100 UTC 20 May (Wu and Yanai, 1994)

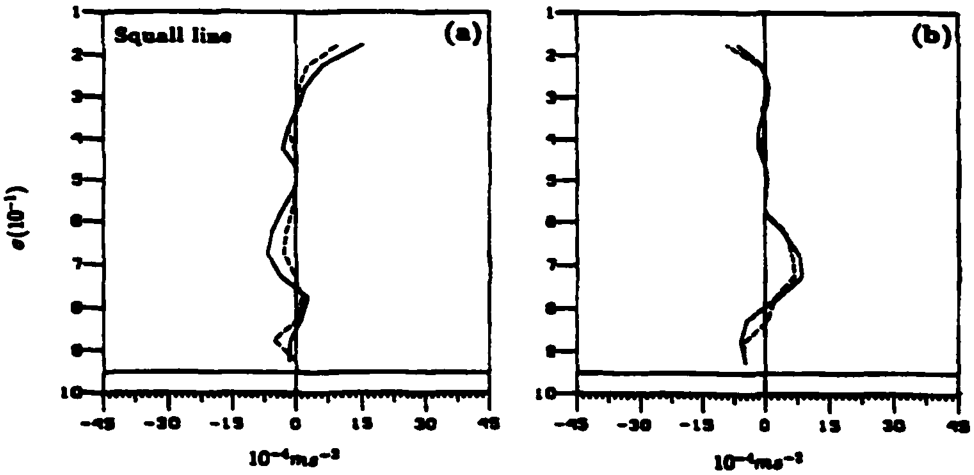

Figure 7: Vertical profiles of (a) line-normal and (b) line-parallel components of observed momentum budget residual (solid) and cumulus-induced acceleration simulated using the cloud momentum model with the convective-scale horizontal pressure-gradient force (Wu and Yanai, 1994).

Kershaw and Gregory (1997a) and Gregory et al. (1997b) developed a parameterization of momentum transport by convection. Using a cloud-resolving model, they investigated two regimes: a mid-latitude cold air outbreak, and tropical convection forced by convergence. They concluded that the convective perturbation pressure-gradient force is proportional to the vertical wind-shear, and to the updraft and downdraft mass-fluxes. This result is consistent with the earlier studies (e. g. Wu and Yanai, 1994). We will also show why this is right in Chapter III. Then, they parameterized the perturbation pressure-gradient force using

$$-\sigma\left(\frac{1}{\rho}\cdot\frac{\partial p'}{\partial x}\right)_{\sigma} = C_{\sigma x}M\left(\frac{\partial \bar{u}}{\partial z}\right), \tag{1.1}$$

and $$-\sigma\left(\frac{1}{\rho}\cdot\frac{\partial p'}{\partial y}\right)_{\sigma} = C_{\sigma y}M\left(\frac{\partial \bar{v}}{\partial z}\right), \tag{1.2}$$

where $C_{\sigma x}$ and $C_{\sigma y}$ are two constants, σ is the area of the system, $M = \rho\sigma\bar{w}_s$ is the mass flux for the system, and $\left(\frac{1}{\rho}\cdot\frac{\partial p'}{\partial x}\right)_{\sigma}$ and $\left(\frac{1}{\rho}\cdot\frac{\partial p'}{\partial y}\right)_{\sigma}$ are the area-mean perturbation pressure-gradient forces in the x and y directions respectively. Also $\bar{u}$ and $\bar{v}$ are the large scale velocity in x and y direction respectively. This parameterization is simple, clear and very easy to understand. As the authors pointed out, the scheme only works well when cloud organization is unimportant.

I-C: Motivation

Though previous studies have provided some information about the vertical transport of horizontal momentum by convection, its parameterization is still an unsolved problem. For example, the cloud-scale pressure-gradient force is not well understood. The aspect ratio, orientation, and phase speed are very important for the perturbation pressure-gradient force, but there is no method to calculate them in current parameterizations.

So, the objectives of this dissertation are: 1) to propose a cumulus momentum transport parameterization that includes the effects of the convective-scale horizontal pressure-gradient force, 2) to develop a method to determine the orientation, aspect ratio, size and propagation speed of the organized convection, 3) to determine the effects of cumulus momentum transport on the environmental wind field, and 4) to determine the effects of shear production on the cumulus convection through including the shear production term in the convective kinetic energy (CKE) equation.

Chapter II: Modification of the environmental flow by cumulus clouds

Now we derive an expression for the effects influencing the environment flow by cumulus clouds. For one type of cloud at a given level, the large-scale effect of momentum transported by cumulus clouds is represented by

$$\frac{d}{dt}\bar{\boldsymbol{v}} = \boldsymbol{F}_c = -\frac{1}{\rho}\frac{\partial}{\partial z}(\rho\overline{\boldsymbol{v}'w'}) = -\frac{1}{\rho}\frac{\partial}{\partial z}[M_c(\boldsymbol{v}_c-\bar{\boldsymbol{v}})], \qquad (2.1)$$

where $M_c = \rho_c\sigma_c w_c$ is the vertical mass flux associated with the cumulus clouds; σ_c is the fractional area covered by the cumulus updrafts; $\boldsymbol{v}_c$ and $\bar{\boldsymbol{v}}$ are the updraft-mean velocity and the large scale wind. $\boldsymbol{F}_c$ was first used in a GCM by Arakawa et al. (1974), and was called "cumulus friction" by Schneider and Lindzen (1976). In (2.1), we show only one cloud type. Actually many cloud types are allowed in our model.

Assuming that there is no local storage of mass and momentum inside an individual cumulus cloud, the flux form continuity equation and momentum equation are

$$\frac{\partial M_c}{\partial z} = E - D, \qquad (2.2)$$

$$\frac{\partial(M_c\boldsymbol{v}_c)}{\partial z} = E\bar{\boldsymbol{v}} - D_c\boldsymbol{v}_c - \frac{\sigma_c}{\rho}\nabla p_c, \tag{2.3}$$

where D represents detrainment. Substituting (2.2) into the left-hand side of (2.3), we obtain

$$\frac{\partial u_c}{\partial z} = \frac{E}{M_c}(\bar{u} - u_c) - \frac{\sigma_c}{\rho M_c}\nabla p_c \tag{2.4}$$

Substituting (2.4) into left-hand side of (2.1), we find that

$$\boldsymbol{F}_c = D_c(\boldsymbol{V} - \bar{\boldsymbol{V}}) + M_c\frac{\partial \bar{\boldsymbol{v}}}{\partial z} + \sigma_c\frac{1}{\rho}\nabla p_c. \tag{2.5}$$

The first term on the right-hand side of (2.5) represents the detrainment of momentum from the cumulus clouds to the environment. The second term represents vertical advection by the environmental subsidence induced by the cumulus clouds. The third term represents the cloud-scale perturbation pressure-gradient force. Suppose that the flow in the lower troposphere has a smaller velocity, and the flow in the upper troposphere has a larger velocity, then subsidence will bring the larger momentum of the upper troposphere down, while the updraft brings the lower-momentum air to the upper troposphere, where it is detrained. So the major effect of the first two terms is a kind of mixing, and downgradient vertical momentum transport is caused by these two effects in many cases. Because the detrainment rate and the cloud mass flux can be determined in terms of the large-scale variables (Arakawa and Schubert 1974), the momentum flux parameterization is reduced to determining the horizontal velocity of the detrained air and the convective-scale pressure-gradient force.

Chapter III: Perturbation pressure-gradient force

The ideas presented here are an extension of the work of Wu and Yanai (1994), Yau (1979) and Holton (1973). Neglecting the Coriolis and the friction terms, a diagnostic pressure equation can be derived under the anelastic approximation:

$$\begin{aligned}-\nabla^2 p' &= 2\rho\left(\frac{\partial\bar{u}}{\partial z}\frac{\partial w}{\partial x}+\frac{\partial\bar{v}}{\partial z}\frac{\partial w}{\partial y}\right)+\rho\left[\left(\frac{\partial u'}{\partial x}\right)^2+\left(\frac{\partial v'}{\partial y}\right)^2+\left(\frac{\partial w}{\partial z}\right)^2\right]\\ &+2\rho\left[\frac{\partial u'}{\partial z}\frac{\partial w}{\partial x}+\frac{\partial v'}{\partial z}\frac{\partial w}{\partial y}+\frac{\partial u'}{\partial y}\frac{\partial v'}{\partial x}\right]-\frac{\partial\rho B}{\partial z}+\frac{w^2}{\rho}\left(\frac{\partial\rho}{\partial z}\right)^2-w^2\frac{\partial^2\rho}{\partial z^2}\ .\end{aligned} \tag{3.1}$$

Here $\nabla^2 = \frac{\partial^2}{\partial x^2}+\frac{\partial^2}{\partial y^2}+\frac{\partial^2}{\partial z^2}$, $\bar{u}$ and $\bar{v}$ are the horizontal components of the environmental wind, w is the vertical velocity, and ρ is the air density. u' and v' are the cloud-scale perturbation velocity components, $u' = u-\bar{u}$, $v' = v-\bar{v}$, where u and v are the horizontal components of the mesoscale wind. $B \equiv g\frac{T_v-\overline{T_v}}{\overline{T_v}}$ is the buoyancy, where T_v is the virtual temperature for the clouds and $\overline{T_v}$ is the virtual temperature of the environment. The first two terms on the right-hand side of (3.1) are due to the effects of the vertical wind-shear. The following six terms are nonlinear. The ninth term is the vertical gradient of the buoyancy. The last two terms are due to the vertical change of the density. We can write

$$p' = p'_{shear} + p'_{nonlinear} + p'_{buoyancy} + p'_{density}. \tag{3.2}$$

In order to calculate the perturbation pressure-gradient force, we consider organized convective clouds as shown in Fig. 8. The clouds are assumed to be organized in the shape of an ellipse which makes an angle θ with the x-axis. This is a mesoscale system with individual convective clouds embedded in it. The derivation below applies to a "smoothed" mesoscale envelope of the convection, so that individual convective cells are not represented. By adjusting the length of the major and minor axes of the ellipse, we can make the elliptical cloud system represent either a linear or a nonlinear MCS.

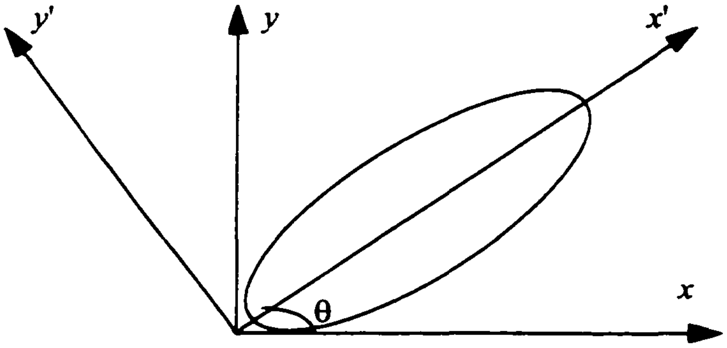

Figure 8: Shape of the organized convective clouds (general case)

For this system, we assume that the shape of the vertical velocity distribution is

$$w = \hat{w}\sin kx'\sin ly'\sin mz \quad , 0 \le \quad kx', ly', mz \le \pi , \qquad (3.3)$$

where $\hat{w}$ is the maximum mesoscale vertical velocity within the ellipse and k, l and m are the wave numbers characterizing the scales of the organized convective mesoscale system. At the upper and lower boundaries, $w = 0$ m s^{-1}. Equation (3.3) assumes a smooth, rounded profile for the vertical velocity inside the mesoscale region. At the center of the ellipse (see Fig. 9a; it is only approximately an ellipse), the vertical velocity is the largest. It becomes smaller away from the center of the ellipse. At the boundary of the ellipse, $w' \approx 0$ m s^{-1}. At the boundary of the rectangular box ($0 \le \quad kx', ly' \le \pi$), $w' = 0$ m s^{-1}. We also assume that the mesoscale horizontal velocity distribution is described by:

$$u' = v_0(z)\cos(kx')\sin(ly')\cos(mz) \ , 0 \le \quad kx', ly', mz \le \pi , \qquad (3.4)$$

$$v' = v_0(z)\sin(kx')\cos(ly')\cos(mz) \ , 0 \le \quad kx', ly', mz \le \pi . \qquad (3.5)$$

In (3.4) and (3.5), $v_0(z)$ is the magnitude of the mesoscale horizontal velocity. At the boundary of the mesoscale system, u' and v' are assumed to be continuous. Lower-level convergence (Fig. 9 c) and upper-level divergence (Fig. 9b) can occur with this kind of horizontal velocity distribution. Substituting (3.3), (3.4) and (3.5) into the continuity equation, i. e.

$$\frac{\partial u'}{\partial x} + \frac{\partial v'}{\partial y} + \frac{\partial w}{\partial z} + \frac{1}{\rho}\frac{\partial \rho}{\partial z}w = 0 , \qquad (3.6)$$

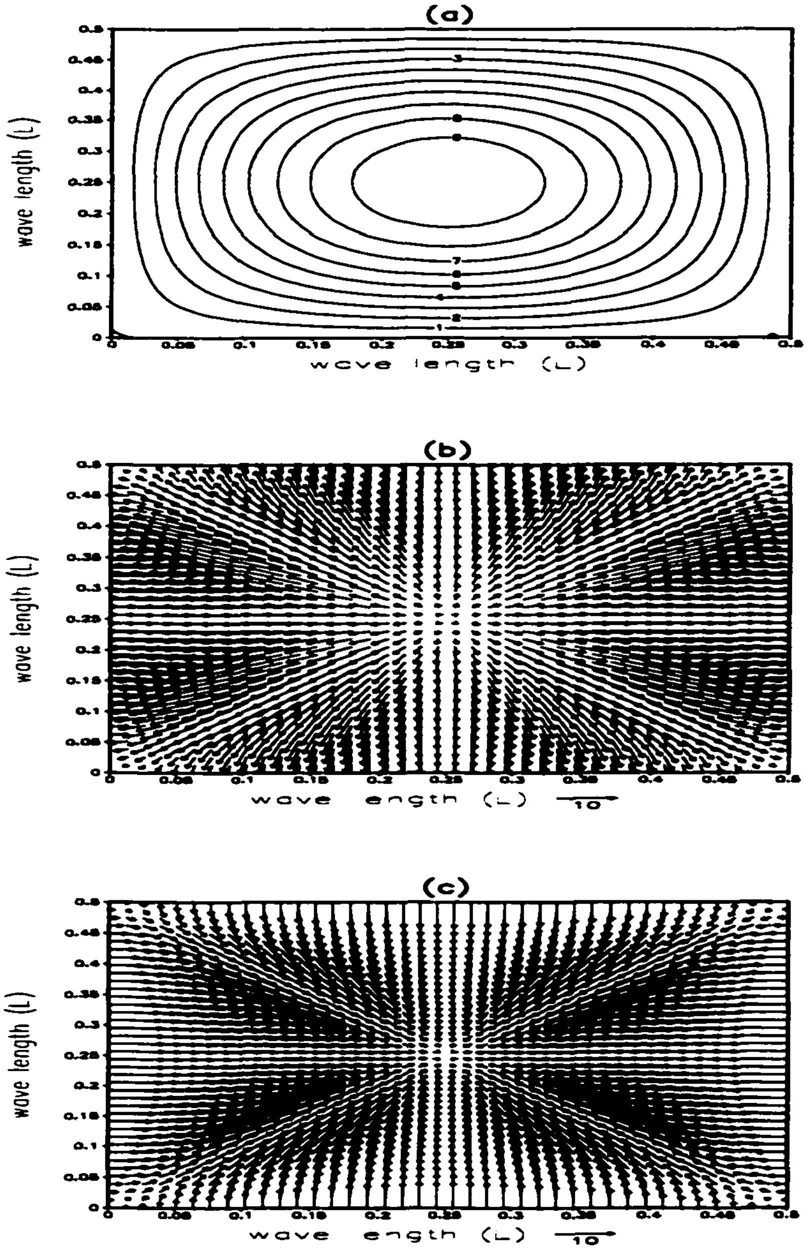

Figure 9: Plots of (a) the vertical velocity (m s^{-1}) at the middle layer, (b) vectors for the horizontal velocity at the upper layer and (c) vectors for the horizontal velocity at the lower layer. The velocities are on the order of 10 m s^{-1}.

we find that:

$$v_0(z) = \frac{\hat{w}\left[m + \frac{1}{\rho}\frac{\partial \rho}{\partial z}\tan(mz)\right]}{k + l} \, . \qquad (3.7)$$

We now substitute (3.3), (3.4), (3.5) and (3.7) into the terms on the right-hand side of (3.1), in order to derive expressions for the perturbation pressure-gradient force. First, substituting (3.3) into the first two terms of (3.1), we obtain an expression for p'_{shear}:

$$\frac{p'_{shear}}{\rho} = \frac{2}{(k^2 + l^2 + m^2)}\left[\frac{\partial \bar{u}}{\partial z}k\cos(kx')\sin(ly') + \frac{\partial \bar{v}}{\partial z}l\sin(kx')\cos(ly')\right]\hat{w}\sin(mz) \, . \qquad (3.8)$$

According to (3.8), this component of the perturbation pressure depends on the vertical wind-shear, the vertical wind speed and the orientation of the system. An expression for the pressure-gradient force can be derived from :

$$-\sigma\left(\frac{1}{\rho} \cdot \frac{\partial p'}{\partial x'}\right)_{\sigma,\, shear} = \frac{v_k}{\rho} \cdot \left(\frac{\partial \bar{u}}{\partial z}\right)M \, , \qquad (3.9)$$

$$-\sigma\left(\frac{1}{\rho} \cdot \frac{\partial p'}{\partial y'}\right)_{\sigma,\, shear} = \frac{v_l}{\rho} \cdot \left(\frac{\partial \bar{v}}{\partial z}\right)M \, , \qquad (3.10)$$

$$-\sigma\left(\frac{1}{\rho} \cdot \frac{\partial p'}{\partial z}\right)_{\sigma,\, shear} = 0 \, . \qquad (3.11)$$

Here $\mathrm{v}_k = \dfrac{2k^2}{k^2+l^2+m^2}$, $\mathrm{v}_l = \dfrac{2l^2}{k^2+l^2+m^2}$, and $M = \rho\sigma\bar{w}_s$ is the mass flux for this system, where σ is the area of the system and $\bar{w}_s = \dfrac{4 \times 3.86}{\pi^3}\hat{w}\sin(mz)$ is the area-average vertical velocity (Appendix). The notation $(\ )_\sigma$ denotes an area average over the ellipse. Equations (3.9) and (3.10) are the same as those derived by Wu and Yanai (1994), but their result was applied to an ensemble of cumulus clouds.

Now substitute (3.3), (3.4), (3.5) and (3.7) into the nonlinear terms on the right-hand side of (3.1). The result is

$$
\begin{aligned}
p'_{nonlinear} = \Big\{ & \rho[v_0^2(k^2+l^2)+\hat{w}^2m^2](\sin kx'\sin ly'\cos mz)^2 \\
& -2\rho v_0 mk\hat{w}(\cos kx'\sin ly'\sin mz)^2 + 2\rho v_0[-ml\hat{w}(\sin kx'\cos ly'\sin mz)^2 \\
& + klv_0(\cos kx'\cos ly'\cos mz)^2]\Big\}/((k^2+l^2+m^2)) \quad .
\end{aligned}
\tag{3.12}
$$

This gives an expression for the perturbation pressure-gradient force due to nonlinear effects:

$$
-\sigma\left(\frac{1}{\rho}\cdot\frac{\partial p'}{\partial x'}\right)_{\sigma,\ nonlinear} = 0 \ , \tag{3.13}
$$

$$
-\sigma\left(\frac{1}{\rho}\cdot\frac{\partial p'}{\partial y'}\right)_{\sigma,\ nonlinear} = 0 \ , \tag{3.14}
$$

$$
\begin{aligned}
-\sigma\left(\frac{1}{\rho}\cdot\frac{\partial p'}{\partial z}\right)_{\sigma,\,nonlinear} &= \left[\frac{\sigma}{3.69\rho(k^2+l^2+m^2)}\right][\\
&[1.19(k^2+l^2)+0.95kl]\frac{\partial\rho v_0^2 cos^2 mz}{\partial z} \\
&+1.19\hat{w}^2 m^2\frac{\partial\rho cos^2 mz}{\partial z}-2wm(k+l)\frac{\partial\rho v_0 sin^2 mz}{\partial z}\Bigg] \quad .
\end{aligned}
\tag{3.15}
$$

We see from (3.13) and (3.14) that for this kind of velocity distribution, the perturbation horizontal pressure-gradient force due to the nonlinear effects is zero. The nonlinear effects do contribute to the vertical component of the perturbation pressure-gradient force.

For the buoyancy term, we assume that $B = B_0(z)\sin(kx')\sin(ly')$, and substitute into (3.1):

$$
p'_{buoyancy} = \frac{\sin(kx')\sin(ly')}{(k^2+l^2+m^2)}\frac{\partial(\rho B_0)}{\partial z} . \tag{3.16}
$$

An expression for the perturbation pressure-gradient force due to the buoyancy term can be derived as follows:

$$
-\sigma\left(\frac{1}{\rho}\cdot\frac{\partial p'}{\partial x'}\right)_{\sigma,\,buoyancy} = 0 \ , \tag{3.17}
$$

$$
-\sigma\left(\frac{1}{\rho}\cdot\frac{\partial p'}{\partial y'}\right)_{\sigma,\,buoyancy} = 0 \ , \tag{3.18}
$$

$$-\sigma\left(\frac{1}{\rho}\cdot\frac{\partial p'}{\partial z}\right)_{\sigma,\,buoyancy} = \frac{4.92\sigma}{\pi^2(k^2+l^2+m^2)}\frac{1}{\rho}\frac{\partial^2(\rho B_0)}{\partial z^2}\,. \tag{3.19}$$

This shows that the buoyancy force has no effects on the perturbation horizontal pressure-gradient force, but does affect the perturbation vertical pressure-gradient force.

Finally, substitute (3.3) into the last two terms (the density-variation terms) on the right-hand side of (3.1) to obtain:

$$p'_{density} = \frac{\hat{w}^2 \sin^2 kx' \sin^2 ly' \sin^2 mz}{(k^2+l^2+m^2)}\left[\frac{1}{\rho}\left(\frac{\partial\rho}{\partial z}\right)^2 - \frac{\partial^2\rho}{\partial z^2}\right]\,. \tag{3.20}$$

This leads to:

$$-\sigma\left(\frac{1}{\rho}\cdot\frac{\partial p'}{\partial x'}\right)_{\sigma,\,density} = 0\,, \tag{3.21}$$

$$-\sigma\left(\frac{1}{\rho}\cdot\frac{\partial p'}{\partial y'}\right)_{\sigma,\,density} = 0\,, \tag{3.22}$$

$$-\sigma\left(\frac{1}{\rho}\cdot\frac{\partial p'}{\partial z}\right)_{\sigma,\,density} = \frac{\sigma}{(k^2+l^2+m^2)}\frac{\hat{w}^2}{3.1\rho}\frac{\partial\left\{\sin^2 mz\left[\frac{1}{\rho}\left(\frac{\partial\rho}{\partial z}\right)^2 - \frac{\partial^2\rho}{\partial z^2}\right]\right\}}{\partial z}\,. \tag{3.23}$$

We see that the density variations do not affect the horizontal perturbation pressure-gradient force, but do affect the vertical perturbation pressure-gradient force.

All of the above formulae have been derived in (x', y') coordinates. We need an expression in (x, y) coordinates. The vertical perturbation pressure-gradient force need not be changed. The horizontal perturbation pressure-gradient force is transformed to:

$$-\sigma\left(\frac{1}{\rho}\cdot\frac{\partial p'}{\partial x}\right)_{\sigma} = \frac{\nu_k}{\rho}\cdot\left(\frac{\partial \bar{u}}{\partial z}\right)M\cos\theta - \frac{\nu_l}{\rho}\cdot\left(\frac{\partial \bar{v}}{\partial z}\right)M\sin\theta\,, \qquad (3.24)$$

$$-\sigma\left(\frac{1}{\rho}\cdot\frac{\partial p'}{\partial y}\right)_{\sigma} = \frac{\nu_k}{\rho}\cdot\left(\frac{\partial \bar{u}}{\partial z}\right)M\sin\theta + \frac{\nu_l}{\rho}\cdot\left(\frac{\partial \bar{v}}{\partial z}\right)M\cos\theta\,. \qquad (3.25)$$

Here θ is the unknown orientation angle. Later we show how to determine this angle.

In contrast to Yau's (1979) approach, our approach describes a mesoscale convective system inside a grid box, while Yau's described individual convective cells. Although we use horizontal and vertical velocity distributions similar to those used by Yau (1979), we use the anelastic approximation in the continuity equation, which is more accurate than the Bousinesq approximation used by Yau (1979).

Chapter IV: The orientation, aspect ratio, and phase speed of the organized convective cumulus clouds

IV-A: Former work

The unknowns in formulae (3.15), (3.19), (3.23), (3.24) and (3.25) are the parameters describing the scale and orientation of the system, i.e. k, l, m, and θ. Little observational and theoretical work has been done on this topic.

Various Richardson numbers (Moncrieff and Green, 1972; Ludlam, 1980; Weisman and Klemp, 1982; Seitter and Kuo, 1983) have been used to classify different types of thunderstorms. Supercell thunderstorms tend to occur for small Richardson numbers, multicell storms for moderate Richardson numbers and air-mass thunderstorms for large Richardson numbers. Using SESAME, PRE-STORM and GATE data, Wu and Yanai (1994) found that large low-level vertical shear is an important factor distinguishing nonlinear MCSs from linear MCSs, although the convective available potential energy also has some influence. The studies mentioned above discuss both dynamic and thermodynamic factors affecting the types of storms. These two classes of factors do influence the organization of convective clouds, but a method is needed to calculate the orientation of organized convection.

Kuo (1963) found that roll-type (linear) convection tends to be parallel to the mean wind for small Richardson numbers. Using a two-dimensional model, Asai (1970) showed that thermal instability is most likely to develop when the wavelength parallel to the basic flow is much longer than that perpendicular to the basic flow. He found that the kinetic energy conversion from mean flow to perturbation flow occurs in this situation. Considering both inertial and thermal instability with a shear flow turning with height, Asai (1972) reported that the preferred unstable perturbation is the convective roll which is aligned with the vertical shear of the basic flow. So Asai tends to support shear-parallel linear MCSs.

Weisman and Klemp (1984)'s work shows that a spectrum of storm types exists, with different types of directionally varying wind-shears: short-lived single cells exist with weak shear, multicell storms with intermediate shear and supercells with strong shear. Their work supports the idea that vertical wind-shear can influence both the strength and organization of the convective systems.

Barnes and Sieckman (1984) classified tropical mesoscale cloud lines occurring in GATE into two different types---fast-movers and slow-movers. For the slow-movers, the principal component of the low-level shear is parallel to the squall line; while for fast-movers the low-level wind-shear lies perpendicular to the squall line. Bluestein and Jain (1985) and Bluestein et al. (1987) noted that Oklahoma convective lines tend to be parallel to the low-level shear. Houz et al. (1990) examined radar reflectivity and raingage data obtained during six springtimes in Oklahoma. About two-thirds of the cases belong to the type of organization in which the convective clouds are arranged along a moving line followed by a region of stratiform cloud; about one-third of the cases belong to chaotic arrangements of convective and stratiform clouds. An evident low-level wind-shear and jet were associated with the cases in which line organization was obvious. Cross-shear (a kind of linear MCS) in the environment is favorable for the squall lines of leading-line/trailing-stratiform structure, which develop quickly. Along-line shear is favorable for squall lines of asymmetric type and the weak degree with leading-line/trailing-stratiform structure. Based on 88 radar-observed linear MCSs, Parker and Johnson (2000) classified convective lines into trailing (TS), leading (LS), and parallel (PS) stratiform precipitations. They found that TS is the dominant mode of linear MCS, while LS and PS composed about 40% of the population studied. Alexander and Young (1992) using the Equatorial Mesoscale Experiment (EMEX) data, LeMone et al. (1998) using TOGA COARE data, and Johnson and Keenan (2001) using South China Sea Monsoon Experiment (SCSMEX) data found that both the low-level and middle-level shear can affect the organization of MCSs. Shear-perpendicular lines tend to develop if the shear exceeds a certain critical value (close to 4 m s^{-1} per 200 mb) at low-levels, and shear-parallel lines tend to develop if the low-level shear is less than the critical value and the middle-level shear (800-400 hPa) exceeds 5 m s^{-1}. When the shear at both levels is large, the orientation of the primary convective band is determined by the low-level shear. The mechanism for the lines perpendicular to the low-level shear is that the convection organizes itself in order to establish a balance between the low-level wind-shear and the cold pool when the low-level shear is very large (Rotunno et al. 1988).

Robe and Emanuel (2001) investigated the effects of vertical wind-shear on the organization of mesocale systems using a three-dimensional cloud ensemble model. They found that the shear at any unstable level has some effects on the organization of the mesoscale systems. When the middle-level shear is strong, shear-parallel lines are favored, but when low-level shear is sufficiently strong, the convection can become very strong and tends to be normal to the shear. The most favorable depth of the low-level shear is the depth of the cold pool. The vertical wind-shear also has significant influence on the thermal structure of the convective clouds. The domain-averaged CAPE first increases and then decreases as the vertical wind-shear increases. At the same time, the lower to middle-level troposphere becomes more humid. Basically, Robe and Emanuel's results are consistent with the diagnostic results mentioned before; however, their results are from a numerical model.

The studies cited above emphasize the importance of vertical wind-shear, especially at low-levels. Their most important findings are that lines can be parallel to or perpendicular to the vertical wind-shear vector. However, they did not give a method to distinguish these two cases.

IV-B: An approach to determine the characteristics of the mesoscale system

We now outline an approach to determine the orientation of the convection. Using the anelastic approximation, the prognostic equations governing the cumulus cloud system can be written as:

$$\frac{\partial u'}{\partial t} + \bar{u}\frac{\partial u'}{\partial x} + \bar{v}\frac{\partial u'}{\partial y} + w'\frac{\partial \bar{u}}{\partial z} + \frac{\partial}{\partial x}\left(\frac{p'}{\bar{\rho}}\right) = 0 \ , \tag{4.1}$$

$$\frac{\partial v'}{\partial t} + \bar{u}\frac{\partial v'}{\partial x} + \bar{v}\frac{\partial v'}{\partial y} + w'\frac{\partial \bar{v}}{\partial z} + \frac{\partial}{\partial y}\left(\frac{p'}{\bar{\rho}}\right) = 0 \ , \tag{4.2}$$

$$\frac{\partial w'}{\partial t} + \bar{u}\frac{\partial w'}{\partial x} + \bar{v}\frac{\partial w'}{\partial y} + \frac{\partial}{\partial z}\left(\frac{p'}{\bar{\rho}}\right) - \frac{\theta'}{\bar{\theta}}g = 0 \ , \tag{4.3}$$

$$\frac{\partial u'}{\partial x} + \frac{\partial v'}{\partial y} + \frac{\partial w'}{\partial z} + \frac{1}{\bar{\rho}}\frac{\partial \bar{\rho}}{\partial z}w' = 0, \tag{4.4}$$

$$\frac{\partial}{\partial t}\left(\frac{\theta'}{\bar{\theta}}\right) + \bar{u}\frac{\partial}{\partial x}\left(\frac{\theta'}{\bar{\theta}}\right) + \bar{v}\frac{\partial}{\partial y}\left(\frac{\theta'}{\bar{\theta}}\right) + \frac{N^2}{g}w' = \dot{\Theta}' . \tag{4.5}$$

Here $\mathbf{v}'$ and θ' are the perturbation momentum and potential temperature, and $\bar{\mathbf{v}}$, $\bar{\theta}$ and $\bar{\rho}$ are the average velocity, potential temperature and the mean density, respectively. N^2 is the Brunt-Vaisalla frequency. $\dot{\Theta}'$ is the perturbation heating and cooling of the cloud due to various processes, such as the cloud microphysical processes, entrainment, detrainment and radiation effects. We assume that $\dot{\Theta}' = \frac{N_0^2 w'}{g}$, where N_0^2 is a function of height.

Combining the two terms of (4.5) that involve w', we get $\frac{N_1^2 w'}{g}$, where the coefficient N_1^2 encompasses the thermodynamic properties of the clouds and the environment, to which the condensation effects contribute a lot. In this paper, we assume that

$$N_1^2 = \frac{g}{\overline{\theta}_e}\frac{\partial\overline{\theta_e}}{\partial z}, \tag{4.6}$$

where $\overline{\theta_e}$ is the equivalent potential temperature of the environment.

To simplify the above equations, we assume that

$$\bar{u} = u_0 + c_{01}(z - z_0) \text{ and } \bar{v} = v_0 + c_{02}(z - z_0), \tag{4.7}$$

where u_0 and v_0 are the components of horizontal velocity at a reference level, z_0 is the height of the reference level, $c_{01} = \frac{\partial\bar{u}}{\partial z}$ and $c_{02} = \frac{\partial\bar{v}}{\partial z}$ are constants. Such quasi-linear horizontal velocity profiles are common in the lower troposphere and are very important for the orientation of organized convective clouds. We also assume that $c_{03} = \frac{1}{\bar{\rho}}\frac{\partial\bar{\rho}}{\partial z}$ is a constant.

We use the WKBJ method (Morse and Feshbach, 1953) to solve (4.1)-(4.5) with the above assumptions. The first step is non-dimensionalization. For convective systems, the following relationships exist:

$$(x, y) = L(x^*, y^*),$$

$$(z) = H(z^*), (u', v', w', \bar{u}, \bar{v}, u_0, v_0) = U(u'^*, v'^*, w'^*, \bar{u}^*, \bar{v}^*, u_0^*, v_0^*),$$

$$(c_{01}, c_{02}) = \alpha(c_{01}^*, c_{02}^*), \frac{p'}{\bar{\rho}} = U^2\frac{p'^*}{\bar{\rho}^*}, \frac{1}{\bar{\rho}}\frac{\partial\bar{\rho}}{\partial z} = \frac{1}{H}\frac{1}{\bar{\rho}^*}\frac{\partial\bar{\rho}^*}{\partial z^*},$$

$$\frac{\theta'}{\bar{\theta}} = \left(\frac{\theta'}{\theta_0}\right)\frac{\theta'^*}{\bar{\theta}^*}, \mu_1^2 = \frac{LN_1^2\theta_0}{g\ \theta'}, t = \frac{L}{U}t^*, \mu_2^2 = \frac{gL\theta_0}{U^2\theta'}. \tag{4.8}$$

Here L and H are used to scale the horizontal and vertical dimensions of the organized mesoscale system respectively, which are assumed to be of the same order. U is the scale for the environmental and cloud velocities. θ_0 is the non-dimensional potential temperature. Superscript "*" denotes a non-dimensional variable, $\alpha = \frac{U}{H}$, $\mu_1^2 \sim 1$, and $\mu_2^2 \sim 1$. Using (4.8) in (4.1)-(4.5), we get:

$$\frac{\partial u'^*}{\partial t^*} + \bar{u}^*\frac{\partial u'^*}{\partial x^*} + \bar{v}^*\frac{\partial u'^*}{\partial y^*} + c_{01}^* w'^* + \frac{\partial}{\partial x^*}\left(\frac{p'^*}{\bar{\rho}^*}\right) = 0, \tag{4.9}$$

$$\frac{\partial v'^*}{\partial t^*} + \bar{u}^*\frac{\partial v'^*}{\partial x^*} + \bar{v}^*\frac{\partial v'^*}{\partial y^*} + c_{02}^* w'^* + \frac{\partial}{\partial y^*}\left(\frac{p'^*}{\bar{\rho}^*}\right) = 0, \tag{4.10}$$

$$\frac{\partial w'^*}{\partial t^*} + \bar{u}^*\frac{\partial w'^*}{\partial x^*} + \bar{v}^*\frac{\partial w'^*}{\partial y^*} + \frac{\partial}{\partial z^*}\left(\frac{p'^*}{\bar{\rho}^*}\right) - \mu_2^2\left(\frac{\theta'^*}{\bar{\theta}^*}\right) = 0, \tag{4.11}$$

$$\frac{\partial u'^*}{\partial x^*} + \frac{\partial v'^*}{\partial y^*} + \frac{\partial w'^*}{\partial z^*} + c_{03}^* w'^* = 0, \tag{4.12}$$

$$\frac{\partial}{\partial t^*}\left(\frac{\theta'^*}{\bar{\theta}^*}\right) + \bar{u}^* \frac{\partial}{\partial x^*}\left(\frac{\theta'^*}{\bar{\theta}^*}\right) + \bar{v}^* \frac{\partial}{\partial y^*}\left(\frac{\theta'^*}{\bar{\theta}^*}\right) + \mu_1^2 w'^* = 0. \tag{4.13}$$

The small parameter used for the WKBJ expansion is $\beta = \frac{h}{L}$, where $z - z_0 = h(z^* - z_0^*)$, and $z - z_0$ is chosen such that β is on the order of 10^{-1}. We can write expansions:

$$u'^* = (u'^*)^{(0)} + \beta(u'^*)^{(1)} + \beta^2(u'^*)^{(2)} + \cdots \tag{4.14}$$

$$v'^* = (v'^*)^{(0)} + \beta(v'^*)^{(1)} + \beta^2(v'^*)^{(2)} + \cdots \tag{4.15}$$

$$w'^* = (w'^*)^{(0)} + \beta(w'^*)^{(1)} + \beta^2(w'^*)^{(2)} + \cdots \tag{4.16}$$

$$\frac{p'^*}{\bar{\rho}^*} = \left(\frac{p'^*}{\bar{\rho}^*}\right)^{(0)} + \beta\left(\frac{p'^*}{\bar{\rho}^*}\right)^{(1)} + \beta^2\left(\frac{p'^*}{\bar{\rho}^*}\right)^{(2)} + \cdots \tag{4.17}$$

$$\frac{\theta'^*}{\bar{\theta}^*} = \left(\frac{\theta'^*}{\bar{\theta}^*}\right)^{(0)} + \beta\left(\frac{\theta'^*}{\bar{\theta}^*}\right)^{(1)} + \beta^2\left(\frac{\theta'^*}{\bar{\theta}^*}\right)^{(2)} + \cdots, \tag{4.18}$$

where the superscipt “(0)” represents the zeroth order approximation, “(1)” the first order approximation, “(2)” the second order approximation, and so on. We also have:

$$\bar{u}^* = 1+\beta(z^* - z_0^*), \tag{4.19}$$

$$\bar{v}^* = 1+\beta(z^* - z_0^*). \tag{4.20}$$

Substituting (4.14)-(4.20) into (4.9)-(4.13), we find that the zeroth-order system is:

$$\frac{\partial u'^*}{\partial t^*} + u_0^*\frac{\partial u'^*}{\partial x^*} + v_0^*\frac{\partial u'^*}{\partial y^*} + c_{01}^* w'^* + \frac{\partial}{\partial x^*}\left(\frac{p'^*}{\bar{\rho}^*}\right) = 0 \ , \tag{4.21}$$

$$\frac{\partial v'^*}{\partial t^*} + u_0^*\frac{\partial v'^*}{\partial x^*} + v_0^*\frac{\partial v'^*}{\partial y^*} + c_{02}^* w'^* + \frac{\partial}{\partial y^*}\left(\frac{p'^*}{\bar{\rho}^*}\right) = 0 \ , \tag{4.22}$$

$$\frac{\partial w'^*}{\partial t^*} + u_0^*\frac{\partial w'^*}{\partial x^*} + v_0^*\frac{\partial w'^*}{\partial y^*} + \frac{\partial}{\partial z^*}\left(\frac{p'^*}{\bar{\rho}^*}\right) - \mu_2^2\left(\frac{\theta'^*}{\bar{\theta}^*}\right) = 0 \ , \tag{4.23}$$

$$\frac{\partial u'^*}{\partial x^*} + \frac{\partial v'^*}{\partial y^*} + \frac{\partial w'^*}{\partial z^*} + c_{03}^* w'^* = 0, \tag{4.24}$$

$$\frac{\partial}{\partial t^*}\left(\frac{\theta'^*}{\bar{\theta}^*}\right) + u_0^*\frac{\partial}{\partial x^*}\left(\frac{\theta'^*}{\bar{\theta}^*}\right) + v_0^*\frac{\partial}{\partial y^*}\left(\frac{\theta'^*}{\bar{\theta}^*}\right) + \mu_1^2 w'^* = 0. \tag{4.25}$$

The dimensional form of equations (4.21)-(4.25) is:

$$\frac{\partial u'}{\partial t} + u_0\frac{\partial u'}{\partial x} + v_0\frac{\partial u'}{\partial y} + c_{01} w' + \frac{\partial}{\partial x}\left(\frac{p'}{\bar{\rho}}\right) = 0 \ , \tag{4.26}$$

$$\frac{\partial v'}{\partial t}+u_0\frac{\partial v'}{\partial x}+v_0\frac{\partial v'}{\partial y}+c_{02}w'+\frac{\partial}{\partial y}\left(\frac{p'}{\bar{\rho}}\right) = 0\ , \tag{4.27}$$

$$\frac{\partial w'}{\partial t}+u_0\frac{\partial w'}{\partial x}+v_0\frac{\partial w'}{\partial y}+\frac{\partial}{\partial z}\left(\frac{p'}{\bar{\rho}}\right)-\frac{\theta'}{\bar{\theta}}g = 0\ , \tag{4.28}$$

$$\frac{\partial u'}{\partial x}+\frac{\partial v'}{\partial y}+\frac{\partial w'}{\partial z}+c_{03}w' = 0, \tag{4.29}$$

$$\frac{\partial}{\partial t}\left(\frac{\theta'}{\bar{\theta}}\right)+u_0\frac{\partial}{\partial x}\left(\frac{\theta'}{\bar{\theta}}\right)+v_0\frac{\partial}{\partial y}\left(\frac{\theta'}{\bar{\theta}}\right)+\frac{N_1^2}{g}w' = 0, \tag{4.30}$$

From the above analysis, we know that (4.26)-(4.30) apply only near the reference level, where $|z-z_0|$ is not too large, but as discussed earlier, previous studies suggest that the orientation of organized cumulus clouds can be determined in this domain. The reference level must satisfy two conditions: 1) it is unstable and 2) it has strong vertical wind-shear. If we assume that the orientation of the clouds does not change with height (this is almost always true), this set of equations can be used to meet our goal. Although we are using only the zeroth-order approximation, we know from the principles of the WKBJ method that the difference between the zeroth-order solution and the full solution is sufficiently small if the first-order terms are smaller than the zeroth-order terms.

We seek solutions of the form:

$$\begin{bmatrix} u' \\ v' \\ w' \\ p' \\ \theta' \end{bmatrix} = \begin{bmatrix} \hat{u} \\ \hat{v} \\ \hat{w} \\ \hat{p} \\ \hat{\theta} \end{bmatrix} \exp i(kx' + ly' + mz - \omega t), \; 0 \le \quad kx', ly', mz \; \le \pi . \tag{4.31}$$

Substitute (4.31) into (4.26)-(4.30). After some mathematical manipulations, we find that:

$$\hat{w}\left\{\left(\frac{1}{\bar{\rho}}\frac{\partial\bar{\rho}}{\partial z} - \frac{k\frac{\partial\bar{u}}{\partial z} + l\frac{\partial\bar{v}}{\partial z}}{k\bar{u} + l\bar{v} - \omega}\right) + i\left[\frac{k^2 + l^2 + m^2}{m} - \frac{{N_1}^2(k^2 + l^2)}{m(k\bar{u} + l\bar{v} - \omega)^2}\right]\right\} = 0 . \tag{4.32}$$

For nontrivial solutions:

$$\begin{gathered} \frac{1}{\bar{\rho}}\frac{\partial\bar{\rho}}{\partial z}(k\bar{u} + l\bar{v} - \omega)^2 - \left(k\frac{\partial\bar{u}}{\partial z} + l\frac{\partial\bar{v}}{\partial z}\right)(k\bar{u} + l\bar{v} - \omega) + \\ i\left[\frac{k^2 + l^2 + m^2}{m}(k\bar{u} + l\bar{v} - \omega)^2 - \frac{N_1^2(k^2 + l^2)}{m}\right] = 0 \quad . \end{gathered} \tag{4.33}$$

We distinguish two types of solutions:

Type I: ω is real. From (4.33) we obtain:

$$N_1^2 = \frac{k^2 + l^2 + m^2}{k^2 + l^2}(k\bar{u} + l\bar{v} - \omega)^2, \tag{4.34}$$

$$\frac{1}{\bar{\rho}}\frac{\partial\bar{\rho}}{\partial z}(k\bar{u} + l\bar{v} - \omega) - \left(k\frac{\partial\bar{u}}{\partial z} + l\frac{\partial\bar{v}}{\partial z}\right) = 0 . \tag{4.35}$$

From (4.34), we see that N_1^2 is greater than or equal to 0. For thermal instability to occur, N_1^2 must always less than 0 before the cumulus processes begin. The cumulus processes can not make N_1^2 too much greater than 0, because otherwise the convection will stop. Before the convection begins, N_1^2 can not be much less than 0, because otherwise $N_1^2 < 0$ will continue for some time. For these reasons, we expect that $N_1^2 \approx 0$ in this case. This is consistent with our assumption that ω is real. From (4.34), we conclude that

$$k\bar{u} + l\bar{v} - \omega \approx 0 . \tag{4.36}$$

Using $\omega = c\sqrt{k^2 + l^2}$, we can calculate the phase speed of the organized clouds:

$$c \approx \frac{ku_0 + lv_0}{\sqrt{k^2 + l^2}} . \tag{4.37}$$

From (4.37), we see that the phase speed is approximately determined by the environmental wind and the organization of the clouds. For a linear MCS, the line normal velocity component contributes more to the phase speed of the mesoscale system, because the wave number in this direction is much larger than that in line parallel direction. Because $k\bar{u} + l\bar{v} - \omega \approx 0$, we see that for (4.35) to be satisfied, we need $k\frac{\partial \bar{u}}{\partial z} + l\frac{\partial \bar{v}}{\partial z} \approx 0$.

Using $L_x = \frac{2\pi}{k}$, $L_y = \frac{2\pi}{l}$, we obtain

$$\frac{L_x}{L_y} \approx \left|\frac{\frac{\partial \bar{u}}{\partial z}}{\frac{\partial \bar{v}}{\partial z}}\right| . \tag{4.38}$$

In case $\left|\frac{\partial \bar{u}}{\partial z}\right| \gg \left|\frac{\partial \bar{v}}{\partial z}\right|$ $\left(\left|\frac{\partial \bar{u}}{\partial z}\right| \ll \left|\frac{\partial \bar{v}}{\partial z}\right|\right)$, $L_x \gg L_y (L_x \ll L_y)$. What this means is that the wind-shear is parallel to the line. For $\left|\frac{\partial \bar{u}}{\partial z}\right| \sim \left|\frac{\partial \bar{v}}{\partial z}\right|$, we have a nonlinear MCS.

Type II: ω is complex. In this case, the convection is growing, so we expect that N_1^2 is less than 0. From (4.33), we find that:

$$\begin{aligned} &\left[\frac{m}{\bar{\rho}}\frac{\partial \bar{\rho}}{\partial z} + (k^2 + l^2 + m^2)i\right](k\bar{u} + l\bar{v} - \omega)^2 \\ &-m\left(k\frac{\partial \bar{u}}{\partial z} + l\frac{\partial \bar{v}}{\partial z}\right)(k\bar{u} + l\bar{v} - \omega) - iN_1{}^2(k^2 + l^2) = 0 . \end{aligned} \tag{4.39}$$

Because $\frac{m}{\bar{\rho}}\frac{\partial \bar{\rho}}{\partial z} \sim 6.28 \times 10^{-8}\mathrm{m}^{-2}$ and $(k^2 + l^2 + m^2) \sim 1.18 \times 10^{-6}\mathrm{m}^{-2}$, we can neglect $\frac{m}{\bar{\rho}}\frac{\partial \bar{\rho}}{\partial z}$ in (4.39):

$$(k^2 + l^2 + m^2)i(k\bar{u} + l\bar{v} - \omega)^2 - m\left(k\frac{\partial \bar{u}}{\partial z} + l\frac{\partial \bar{v}}{\partial z}\right)(k\bar{u} + l\bar{v} - \omega) - iN_1{}^2(k^2 + l^2) \approx 0 . \tag{4.40}$$

Setting $\omega = \omega_r + \omega_i i$, and solving (4.40), we obtain:

$$\omega_r = ku_0 + lv_0, \tag{4.41}$$

$$\omega_i = \frac{m\left(k\frac{\partial\bar{u}}{\partial z}+l\frac{\partial\bar{v}}{\partial z}\right)+\sqrt{m^2\left(k\frac{\partial\bar{u}}{\partial z}+l\frac{\partial\bar{v}}{\partial z}\right)^2-4N_1^2(k^2+l^2)(k^2+l^2+m^2)}}{2(k^2+l^2+m^2)}, \qquad (4.42)$$

where the decaying solution has been discarded. From (4.41), we get the same phase-speed formula as for Type I, i. e. (4.37). The most rapid growth rate occurs for

$$\frac{\partial\omega_i}{\partial k} = 0, \text{ and} \qquad (4.43)$$

$$\frac{\partial\omega_i}{\partial l} = 0. \qquad (4.44)$$

Substituting (4.42) into (4.43) and (4.44), and letting $a \equiv m\left(k\frac{\partial\bar{u}}{\partial z}+l\frac{\partial\bar{v}}{\partial z}\right)$ and $b^2 \equiv k^2+l^2+m^2$, we get

$$\left[a+\sqrt{a^2-4N_1^2b^2(b^2-m^2)}\right]\left(m\frac{\partial\bar{u}}{\partial z}b-2ka\right) = 4kN_1^2m^2b, \qquad (4.45)$$

$$\left[a+\sqrt{a^2-4N_1^2b^2(b^2-m^2)}\right]\left(m\frac{\partial\bar{v}}{\partial z}b-2la\right) = 4lN_1^2m^2b. \qquad (4.46)$$

From the ratio of (4.45) to (4.46), we find that $l\frac{\partial\bar{u}}{\partial z} = k\frac{\partial\bar{v}}{\partial z}$, so we have

$$\frac{L_x}{L_y} = \left|\frac{\frac{\partial \bar{v}}{\partial z}}{\frac{\partial \bar{u}}{\partial z}}\right|. \tag{4.47}$$

In case $\left|\frac{\partial \bar{u}}{\partial z}\right| \gg \left|\frac{\partial \bar{v}}{\partial z}\right| \left(\left|\frac{\partial \bar{u}}{\partial z}\right| \ll \left|\frac{\partial \bar{v}}{\partial z}\right|\right)$, $L_x \ll L_y (L_x \gg L_y)$. What this means is that the vertical wind-shear is perpendicular to the line. For $\left|\frac{\partial \bar{u}}{\partial z}\right| \sim \left|\frac{\partial \bar{v}}{\partial z}\right|$, we have a nonlinear MCS.

Now we have derived conditions to determine the aspect ratio of the organized cloud system: formula (4.38), which applies when N_1^2 is close to zero; and formula (4.47), which applies when N_1^2 is less than zero. We choose

$$(N_1^2)_{critical} = -5 \times 10^{-5}\ \mathrm{s}^{-2} \tag{4.48}$$

as the threshold value to distinguish these two cases. Tests show that this value works well for GATE, ARM (the Southern Great Plains Site of the Atmospheric Radiation Measurements Project), EMEX, SCSMEX, and TOGA COARE data. However, more experiments are needed for a better determination of this criterion. For N_1^2 close to the critical value, we assume that the mesoscale system is a nonlinear MCS with $L_x = L_y$.

Before continuing the discussion of the orientation of the organized cumulus clouds, we test the theory by applying it to the fast-movers and slow-movers reported by Barnes and Sieckman (1984; all data is available in *Mon. Wea. Rev.*, **112**, 1782-1794). We choose the reference level to be 3 km above the cloud base for two reasons: 1) the two conditions for reference level are satisfied in this level for both the fast-movers and slow-movers, and 2) the horizontal velocity components at this level are the mean value of all the levels satisfying the two conditions.

For the fast-movers, we find that $N_1^2 = -9.3 \times 10^{-5}\ \mathrm{s}^{-2}$ as calculated by (4.6), so this is a Type II case. From (4.47) $\frac{L_P}{L_N} = \left|\frac{\frac{\partial \bar{v}_N}{\partial z}}{\frac{\partial \bar{v}_P}{\partial z}}\right| = 16.1$, where the subscripts P and N refer to variables parallel and normal to the line, respectively. $\bar{v}_N$ and $\bar{v}_P$ are calculated using a linear fit to the low-level wind. Because the ratio of the two wave lengths is greater than 10, we interpret this case as a squall line. This ratio is calculated from a composite vertical wind-shear from three soundings. We do not know the observed aspect ratio, however, this number is realistic for a common squall line. This is a Type II case. The orientation of the squall line is perpendicular to the vertical wind-shear. Using (4.37), we estimate that the phase speed of the squall line was about -12 m s^{-1}. This compares well with the observed speed of -11.1 m s^{-1}.

For the slow-movers, $N_1^2 = -1.86 \times 10^{-5}\ \mathrm{s}^{-2}$, so this is a Type I case. From (4.38), we find that $\frac{L_P}{L_N} = \left|\frac{\frac{\partial \bar{v}_P}{\partial z}}{\frac{\partial \bar{v}_N}{\partial z}}\right| = 12.5$. Again, we regard this as a squall line. Using

(4.37), we estimate that the phase speed of the squall line is -2 m s^{-1}. The observed speed was about -2.2 m s^{-1}.

So our theory can explain the orientation, aspect ratio and phase speed of the GATE fast-movers and slow-movers.

An additional condition is needed to determine the horizontal dimensions of the organized clouds. If the shape of the cloud system is an ellipse, the area is

$$\sigma = \frac{1}{4}\pi L_x L_y . \qquad (4.49)$$

By combining (4.38) or (4.47) with (4.49), we can determine L_x and L_y for the organized cumulus clouds, if the area is known. We assume that the area of the mesoscale region is two orders of magnitude larger than the collective area of the convective updrafts. A method to determine the updraft area is described later.

The vertical wave number of the organized clouds, m, can be calculated from the lower and upper boundary conditions:

$$w'(z=z_B) = 0 , \qquad (4.50)$$

$$w'(z=z_T) = 0 . \qquad (4.51)$$

Here z_T is the highest cloud-top height, and z_B is the lowest cloud-base height of the elliptical system. Substituting (4.31) into (4.50) and (4.51), we find that:

$$m = \frac{\pi}{z_T - z_B}. \tag{4.52}$$

We also need to determine the angle between the linear MCS and the axis. A linear MCS is assumed to be oriented such that it has a maximum or minimum $\frac{L_x}{L_y}$. For example, a fast-mover is oriented such that one of its axes is as large as possible and the other one is as small as possible, from (4.47). For any other orientation of the coordinate, the ratio of the two lengths will be less extreme. The condition for a linear MCS is:

$$\left|\frac{L_x}{L_y}\right| < 0.1 \quad \text{or} \quad \left|\frac{L_x}{L_y}\right| > 10. \tag{4.53}$$

Only one of these conditions can be satisfied.

In summary, we first choose a reference level using the two conditions (for deep clouds, about 2-4 kilometers above cloud base; for shallow clouds, at lower level). Using (4.48), we distinguish Type I from Type II (Table 1). Then a linear fit is used to calculate the low-level wind-shear. We calculate the aspect ratio using (4.38) or (4.47) with (4.49), and distinguish between linear MCSs and nonlinear MCSs using (4.53). Finally, (4.37) is used to calculate the phase speed of the convective system.

Table 1: Criterion to distinguish various types of MCSs

	$\left\|N_1^2\right\|$ s^{-2}	vertical wind-shear
Linear MCSs Type II	$\left\|N_1^2\right\| > 5\times10^{-5}$	$\left\|\frac{L_T}{L_P}\right\| < 0.1$ or $\left\|\frac{L_P}{L_T}\right\| > 10$
Linear MCSs Type I	$\left\|N_1^2\right\| < 5\times10^{-5}$	$\left\|\frac{L_T}{L_P}\right\| < 0.1$ or $\left\|\frac{L_P}{L_T}\right\| > 10$
Linear MCSs no preferred orientation	$\left\|N_1^2\right\| \approx 5\times10^{-5}$	$\left\|\frac{L_T}{L_P}\right\| < 0.1$ or $\left\|\frac{L_P}{L_T}\right\| > 10$
Nonlinear MCSs	unstable	$\left\|\frac{L_T}{L_P}\right\| > 0.1$ or $\left\|\frac{L_P}{L_T}\right\| < 10$

Our approach is consistent with the previous work, and also represents some progress. We use the thermodynamic condition (4.48) to distinguish the two cases: a line normal to the vertical wind-shear and a line parallel to the vertical wind-shear. The vertical wind-shear is used to determine the aspect ratio of the line. We have also given a method to determine the orientation and the phase speed.

Kuo's (1963) roll-type convection belongs to our Type I. Using an analytical method, he solved equations similar to (4.1)-(4.5) for dry convection with shear only in one direction. He pointed out the Type II is possible when instability is very strong, but he did not discuss this mode further. When Richardson number[3] is between -2 and 0 (weak instability), Type I is favored, because the stabilizing effect of the vertical wind shear is inhibited. In summary, our results are consistent with Kuo's (1963) although his method is very different from ours.

The preferred convectively growing modes reported by Asai (1970, 1972), including both thermal and inertial instability, belong to our Type I. He solved a set of equations similar to (4.1)-(4.5) for dry convection, using a numerical method. He found that the kinetic energy of the mean wind can be converted to convective kinetic energy for Type I, and that the growth rate of this mode is large. In his experiments, he only considered Richardson numbers[4] between 0 and 2. I have calculated the N_1^2s for these cases, and they are larger than $-5 \times 10^{-5}\ s^{-2}$. Comparing his approach with ours, we use a different method in the weak instable region and get the same result. However, he did not consider cases for which the Richardson number is greater than 2.

To summarize the above discussions, we give a comparison between the earlier approaches and ours in Table 2.

---

[3] Defined as the ratio of the vertical potential temperature gradient and the vertical wind shear

[4] Same as that of Kuo(1963), except opposite sign.

Table 2: Comparison of our approach with those of Kuo (1963) and Asai (1970, 1972)

	Kuo (1963)	Asai (1970 and 1972)	Current study
Instability	Dry	Dry	Wet (simplified)
Shear	Shear in one direction	Shear turning with height	Shear turning with height
Method	Power series and asymptotic approximations	Numerical solution	WKBJ method
Results	A growing parallel mode	A growing parallel mode	A parallel mode (can grow) and a normal mode (growing fast)

The results of our theory are consistent with the mechanism proposed by Rotunno et al. (1988), which applies for large $|N_1^2|$ (Type II). Strong downdrafts are associated with large growth rates and CAPE, and smaller θ_e in the upper levels causes a stronger cold pool. So the balance between the strong low-level shear and the cold pool determines the orientation of the line. What this means is that our theory takes the effects of cold pool into consideration implicitly. Type II can produce a strong cold pool, which has positive feedback on Type II.

Our theory applies not only for the whole troposphere, but also for any level of the troposphere. Low-level $|N_1^2|$ (see Alexander and Young, 1992 and LeMone et al. 1998) tends to be large in many cases, so shear-normal linear MCSs of Type II tend to develop for large low-level wind-shear. However, middle-level $|N_1^2|$ tends to be small. Fig. 10 shows typical profiles for equivalent potential temperature for environmental soundings. The instability in the lowest 200 mb is much stronger than that of the middle-levels. As a result, Type I linear MCSs tend to develop with large middle-level shear. This is why shear-parallel linear MCSs tend to develop for large middle-level wind-shear. When both the low-level and middle-shear are large, Type I linear MCSs tend to develop. This is what Alexander and Young (1992), LeMone et al. (1998) and Johnson and Keenan (2001) found.

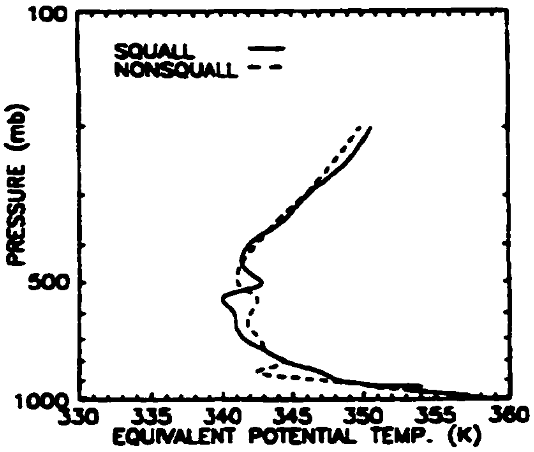

Figure 10: Equivalent potential temperature profiles for the composite environmental soundings (Alexander and Young, 1992).

Johnson and Keenan (2001) found a special case on May 23 12UTC, 1998, in which the low-level shear is parallel to the orientation of the linear MCS. The corresponding equivalent potential temperature sounding is shown on Fig. 11. The hodograph for one of their normal cases (May 19 00UTC, 1998) and this special case is plotted on Fig. 12. The largest wind-shear level for these two cases is between 1 km and 2 km and this level is also unstable, so we choose this level as the reference level. For their normal case, $\left|N_1^2\right| = -8.5\times10^{-5}\ \mathrm{s}^{-2}$, which is much smaller than the critical value. The normal case therefore belongs to Type II. For their special case, $\left|N_1^2\right| = -5\times10^{-6}\ \mathrm{s}^{-2}$, which is much larger than the critical value. The special case therefore belongs to Type I. Although the equivalent potential temperature changes little with height (near neutral) for the line-parallel case, the air at the reference level is not saturated. This maybe due to the strong mixing near the reference level. From the radar images (not shown), we can see that the growth rate for the line-parallel case is very small. This is expected for a Type I linear MCS.

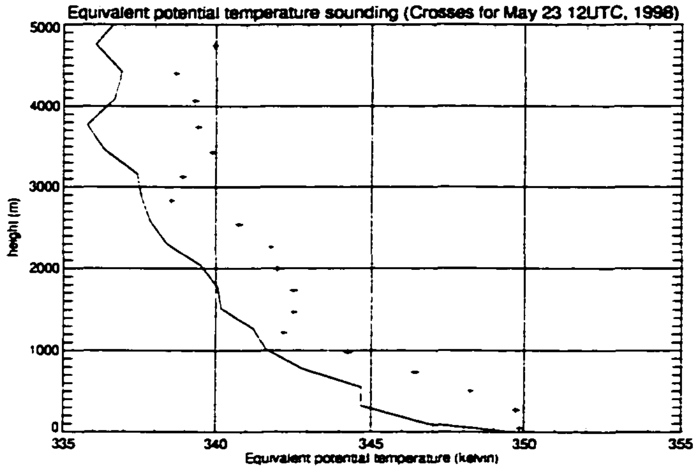

Figure 11: Equivalent potential temperature soundings for Johnson and Keenan's (2001) normal case (line normal to low-level shear) on May 19, 00UTC, 1998 (solid line) and for their special case (line parallel to low-level shear) on May 23, 12 UTC, 1998 (crosses).

For the line-parallel cases, if the shear and low-level jet are mainly in the line-parallel direction, the speed of the line will be small (as with the GATE slow-movers) because the wave number in the line-parallel direction is small. In this case, suppose that the line lies perpendicular to the vertical wind-shear and low-level jet. The line will move pretty fast. This may not be favorable for the line's growth, because as the downdraft moves away, no strong cold pool can be produced, so the positive feedback between the cold pool and low-level shear cannot be established. This might be the physical image: Shear-parallel lines tend to occur when shear-perpendicular lines do not occur.

From the above analysis, we can calculate the orientation, aspect ratio and phase speed of the organized mesoscale system. For our theory to be used in a cumulus parameterization, we need to assume that every cloud type inside the grid box has the same orientation and aspect ratio as the mesoscale system itself. This assumption was used by Wu and Yanai (1994), whose results compared well with observations.

The diagnostic perturbation pressure equation, (3.1), can be applied for the individual cumulus clouds. The vertical velocity profile for the cumulus clouds is assumed to be approximately bell-shaped. However, the magnitude of the cumulus vertical velocity is larger than that of the mesoscale system. So substituting (3.3), (3.4), (3.5) and (3.7) into the terms on the right-hand side of (3.1), we get perturbation pressure-gradient forces for individual cumulus clouds given by (3.15), (3.19), (3.23), (3.24) and (3.25).

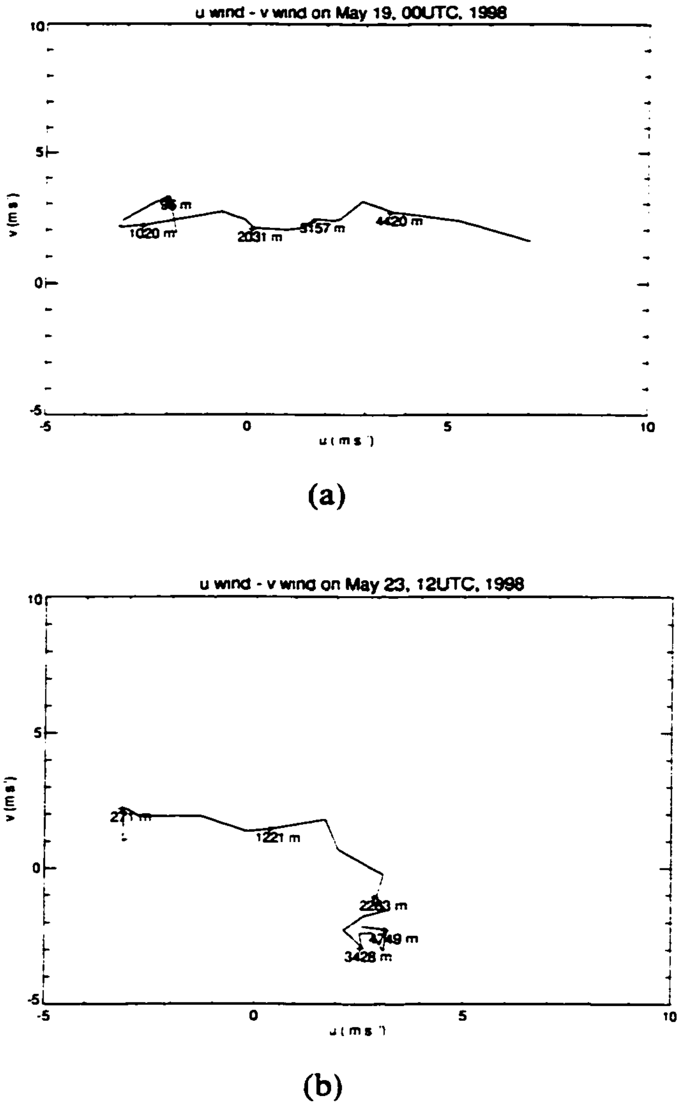

Figure 12: Hodograph for two horizontal wind components (a) on May 19, 00 UTC, 1998 and (b) on May 23, 12 UTC, 1998). The height of some important points are printed right below the crosses.

Chapter V: Simulations

Data and experiment design

The CSU SCM (Colorado State University single column model) is used in this study to investigate the new scheme and convective momentum transport. The SCM uses the same computer code as the CSU GCM except that the SCM runs in one-dimensional mode. The model has 17 levels and uses a stretched vertical coordinate (Suarez et al. 1983). The planetary boundary layer (PBL) is the lowest layer of the model. The depth and the turbulence kinetic energy of the PBL are prognostic variables. The cumulus parameterization is base on Arakawa and Schubert's (1974) ideas, but with prognostic closure (Pan and Randall, 1998) and multiple cloud-bases (Ding and Randall, 1998).There are no downdrafts in this scheme. The stratiform cloud parameterization was developed by Fowler et al. (1996) and Fowler and Randall (1996 a, b). The radiation parameterization is that of Harshvardhan et al. (1987). The surface fluxes of sensible and latent heat are prescribed according to observations (Randall and Cripe, 1999). The "revealed forcing", which specifies the total large-scale advective effects ($-\left(\mathbf{v} \bullet \nabla q + w\frac{\partial q}{\partial p}\right)_{obs}$) directly from the analyzed observations (e. g. Redelsperger et al., 1998; Bechtold et al., 1998), is employed. It is a very simple forcing.

ARM and TOGA COARE data are used to drive the SCM and provide the initial conditions. We also use other ARM and TOGA COARE data for the same period to evaluate the two simulations. The simulations driven with the ARM data set represent the results of our parameterization from middle latitudes, while those driven by TOGA COARE data represent the results of our parameterization from low latitudes.

ARM's Southern Great Plains site is located in north-central Oklahoma and south-central Kansas (Stokes and Schwartz, 1994). Twelve observing stations supply the data for the SCM. The center of the box is at 97.49°W and 36.61°N. A variety of instruments, such as radiosondes and wind profilers, collect data. The data used here are from Intensive Observation periods (IOPs), during which data are collected with increased frequency, and radiosondes are launched from four positions around the site, which coincide with the locations of National Oceanic and Atmospheric Administration wind profilers, and in the center of the site. The precipitation data were provided by the Oklahoma mesonet, Kansas State University mesonet and Surface Meteorological Observing System (SMOS). The data from radiosondes and wind profilers were subjected to objective analysis (Leach et al., 1996, 1997). The wind profiler and radiosonde data were merged using Barnes' (1964) methods.

Lin and Johnson's (1996 a, b) methods are used to analyze the TOGA COARE data. All the wind and thermodynamic data from soundings were analyzed using multiquadratic interpolation (Nuss and Titley, 1994) onto a 1-by-1 degree grid. All the points falling into the Intensive Flux Array (IFA) were averaged together. The center of the box is at 155°E and 2°S. The data used in this study is the intensive observation period (IOP) of the experiment, which was carried out from November 1992 to February 1993 over a broad region of the west Pacific bordered by 10°N, 10°S, 140°E, and the date line. The radar images are from CSU-MIT radar located on the research vessel R/V John V. Vickers (located at 156°E and 2°S) owned by the University of Southern California and operated by the NOAA (National Oceanic and Atmospheric Administration) Corps through 1993. CSU-MIT radar is a C-band radar operating near the 5 cm wavelength band. It is only weakly attenuated by intervening rainfall. Its transmitters are often small and compact, and can operate well with relatively small (8-12') antennas. The radar is an ideal tool for cloud observations.

For ARM data, three kinds of simulations have been made in this dissertation. All simulations started from the same initial condition (17:30 June 18, 1997) and ran 30 days to 17:30 July 18,1997. Every case is integrated nine times with a little change of initial conditions (about 1 ‰ change of initial temperature or 1% change of initial water vapor mixing ratio, see Table 3). We average the results to eliminate the influence of the random errors. One kind of simulation (designated as MR) employs the new cumulus momentum transport scheme introduced here. In the other kind of simulation (the control run, CR), the contribution of the perturbation pressure-gradient force is neglected. Another class of simulations adds the shear production term in the CKE equation (the CKE run). One objective of these simulations is to test the orientation, aspect ratio and phase speed of the convection predicted by the theory. Another objective is to find the frictional force due to the momentum flux associated with the cumulus convection (see Table 4). Comparison of the MR and CR runs will show how much the perturbation pressure-gradient force contributes to the vertical momentum transport. We are also interested in evaluating the contribution that the shear makes in CKE equation.

Table 3: Nine different initial conditions used in SCM (only temperature and water vapor mixing ratio are changed at every level based on T_0 and q_0)

experiment number	T (temperature)	q (mixing ratio)
1	$0.995T_0$	q_0
2	$0.999T_0$	q_0
3	T_0	q_0
4	$1.004T_0$	q_0
5	$1.003T_0$	q_0
6	T_0	$0.98q_0$
7	T_0	$0.99q_0$
8	T_0	$1.01q_0$
9	T_0	$1.02q_0$

Table 4: Three different runs

Experiment	perturbation pressure-gradient force	shear production term	integration times
MR run	included	not included	9
CR run	not included	not included	9
CKE run	included	included	9

For TOGA COARE data, we made CKE and CR runs. The integration period is from November 1, 1992 to February 28, 1993. We will examine the orientation, size, and phase speed for the mesoscale system and vertical momentum transport for the convective clouds for this period.

V-A: Results of numerical simulations

In this section, we present the results of the new parameterization. We will show how the convective-scale pressure-gradient force, produced by the interaction of vertical wind-shear with organized convection, influences the simulated momentum flux.

Let us first see what kind of convective processes occurred during the ARM IOPs. Fig. 13 shows the observed total rain. There are about six precipitation events. We have radar data only from June 18 to June 27, June 30 to July 4, July 9 to July 11 and July 13 to July 15. The stronger events occurred during June 26 and can be seen in the radar data. Both nonlinear and linear MCS can be seen on June 26.

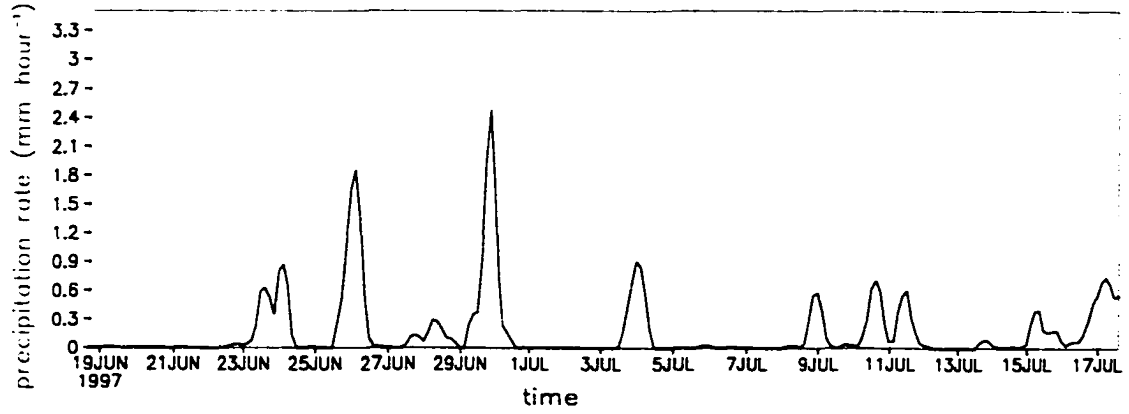

Figure 13: Observed precipitation during the simulation period (mm hour^{-1}).

For TOGA COARE, we have radar images from November 9, 1992 to February 26, 1993, so we can test the simulations in a complete manner.

V-A-1: The orientation of the convection

For both ARM and TOGA COARE simulations, there are several ways in which we can test our theory of organized convection. We choose some cases that can represent the characteristics of the linear MCSs and nonlinear MCSs.

Fig. 14 (a) shows the predicted orientation and phase speed for July 15 12:15,1997 (ARM Case 1). Fig. 14 (b) shows the corresponding observed orientation and phase speed of the squall line. The area for the radar image is about $400\ \text{km} \times 400\ \text{km}$. We estimate the size of the squall line to be $20\ \text{km} \times 230\ \text{km}$ by calculating the length and the wide of the high echo area. Fig. 14 (a) and Fig. 14 (b) are plotted with the same scale. The mesoscale area is calculated by increasing the collective convective cloud area by factor of 200 for a linear MCS and by factor of 400 for a nonlinear MCS (this is reasonable because the updraft core is two orders less than mesoscale system.):

$$\sigma_s \approx 100 \sum_i \sigma_{ci} . \qquad (5.1)$$

Here σ_s is the area of the mesoscale system and σ_{ci} is the area of the cumulus cloud type i. σ_{ci} is calculated by:

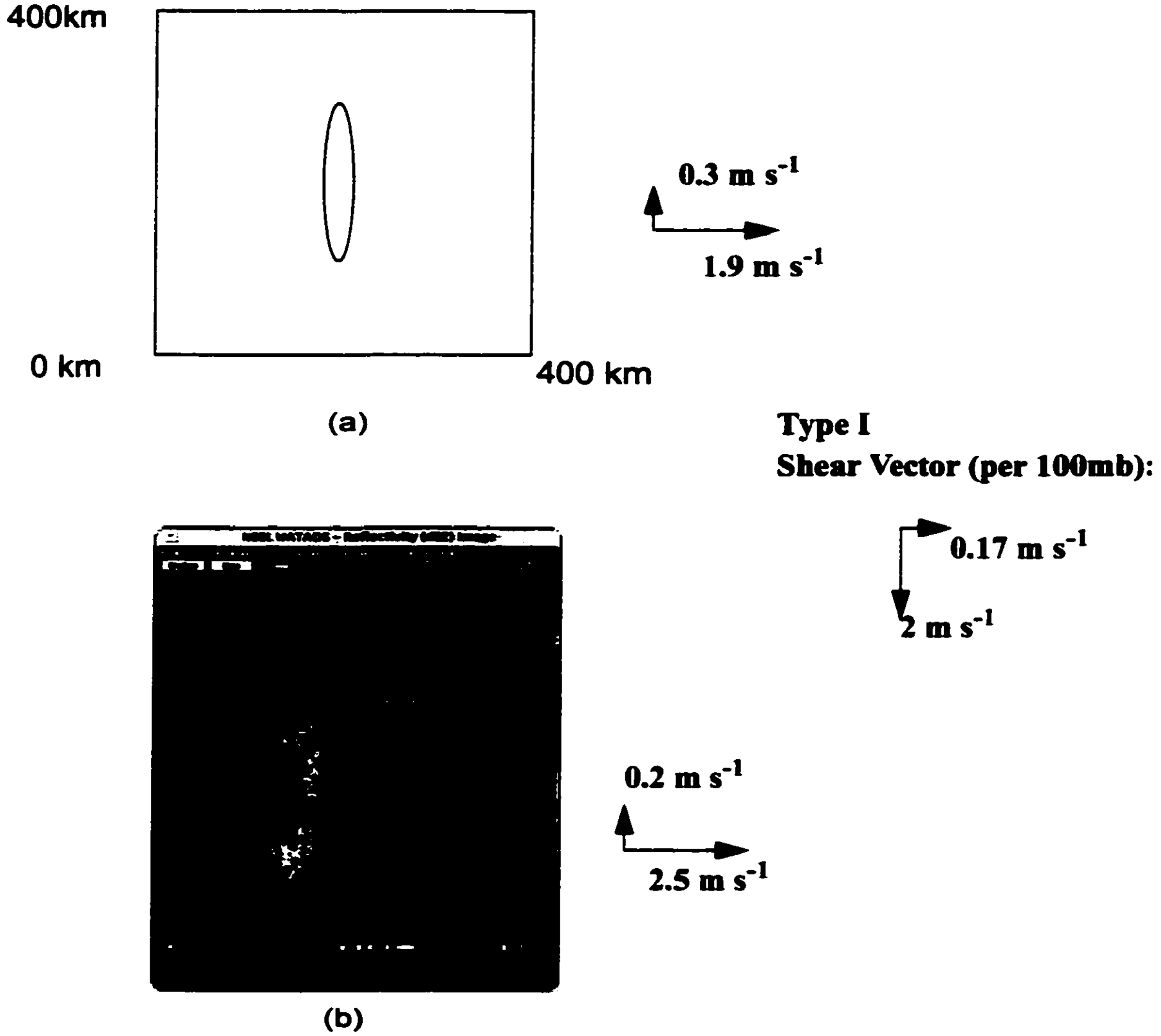

Figure 14: a) Organized cumulus cloud orientation from the theory for July 15, 12:14, 1997 (ARM Case 1), The ellipse's long axis makes an angle of 0° with the y axis. and (b) Observed rain-band.

$$\sigma_{ci} = \frac{M_{ci}}{\rho w_{ci}}. \tag{5.2}$$

w_{ci} can be calculated by the vertical momentum budget of the updraft (Simpson and Wiggert 1969, Cheng 1989a):

$$w_{ci}^2 = \frac{g\left[\frac{\bar{T}_{vi} - T_{ci}}{\bar{T}_{vi}} + l_{ci} + q_{ri}\right]}{f_1(1+\gamma)\left[2\lambda - \frac{1}{\rho_{ci}}\frac{\partial \rho_{ci}}{\partial z}\right]}, \tag{5.3}$$

where T is the temperature, l_c is the liquid water content of cloud, q_{ri} is the rainwater mixing ratio, f_1 is a constant, γ is the virtual mass coefficient, λ is the entrainment rate, and ρ_{ci} is the density of the cloud air. The mass flux M_{ci} is calculated by using prognostic closure (Pan and Randall 1998) with the CKE (Convective Kinetic Energy) equation. The scale of the convective ellipse is about 19.5 km × 259 km from our model. Because an extremely complex iteration is needed to calculate the vertical perturbation pressure-gradient force, we do not use the formulae that we derived to calculate the vertical velocity here. This is a simple case. Only one squall line existed in the box. The orientation of the squall line is close to north-south. The vertical wind-shear in the unstable levels satisfies $\frac{L_y}{L_x} = \left|\frac{\frac{\partial \bar{v}_y}{\partial z}}{\frac{\partial \bar{v}_x}{\partial z}}\right| \gg 1$. This is a case which the vertical wind-shear is parallel to the line. From our theory the phase speed is about 1.9 m s^{-1} normal to the squall line and about -0.3 m s^{-1} parallel to the line. The phase speed of the mesoscale system is calculated from radar-data animations. We printed out the radar images every ten minutes in an hour and tracked the moving of the high echo area. The speed of the mesoscale system is the average speed for an hour. The predicted orientation and speed are in good agreement with the observations.

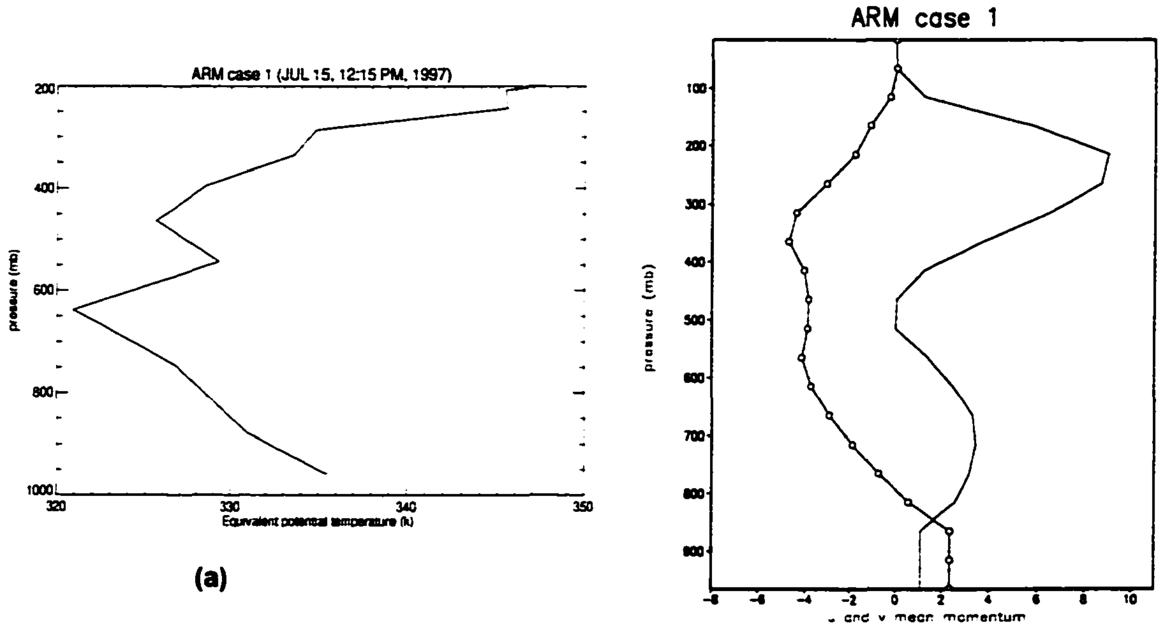

(a)

(b)

Figure 15: (a) Environmental equivalent potential temperature sounding and (b) u (solid line) and v (line with open circles) mean wind for ARM case 1.

Fig. 15 shows the environmental equivalent potential temperature, u, and v wind, which we can used to choose the reference level. From the equivalent potential temperature soundings, we find the reference level can only exist below 450 mb because two instable levels (450mb-550mb and 650mb -950mb) are in this range. The largest shear level occurs between 500mb and 850 mb. Mean wind in y direction does not have linear structure. In order to use our theory, we have to use a linear fit to the v wind. This makes we have to choose the reference level between 500 mb and 850 mb. We choose 650 mb as the reference level since it is in the middle of the largest shear and is unstable.

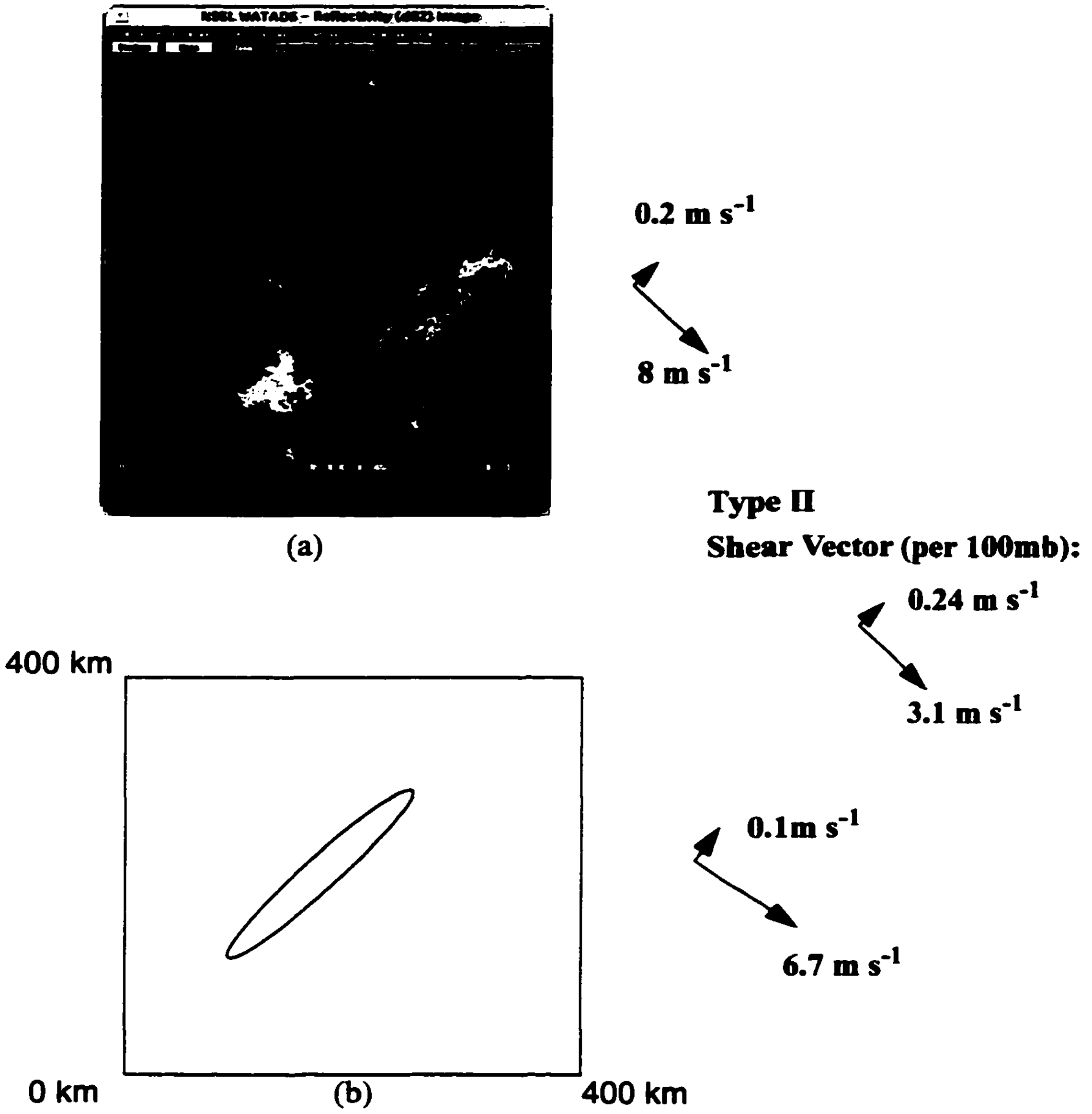

Figure 16: (a) Observed rain-band for June 26, 14:30, 1997 (ARM Case 2) and (b) Organized cumulus cloud orientation from the theory, the ellipse's long axis makes an angle of 45° with the y axis.

Fig. 16 (a) shows the orientation and phase speed of the squall line as seen by radar on June 26, 14:30, 1997 (ARM Case 2). The size of the squall line is estimated to be $20\ \text{km} \times 280\ \text{km}$. Fig. 16 (b) shows the orientation and phase speed from the theory for that time. The scale of the convective ellipse is about $17.6\ \text{km} \times 232\ \text{km}$. The orientations from the theory and the observations agree very well. Both lie in north-east to south-west direction. From theory, the phase speed normal to the squall line is 6.7 m s^{-1}, and parallel to the line is 0.1 m s^{-1}. Compared to the radar data, the line's speed and direction are approximately right. We choose the reference level according Fig. 17. The unstable level is below 600 mb. The level of the strongest shear is between 700 mb and 850 mb, which is also unstable. We choose 750 mb as the reference level.

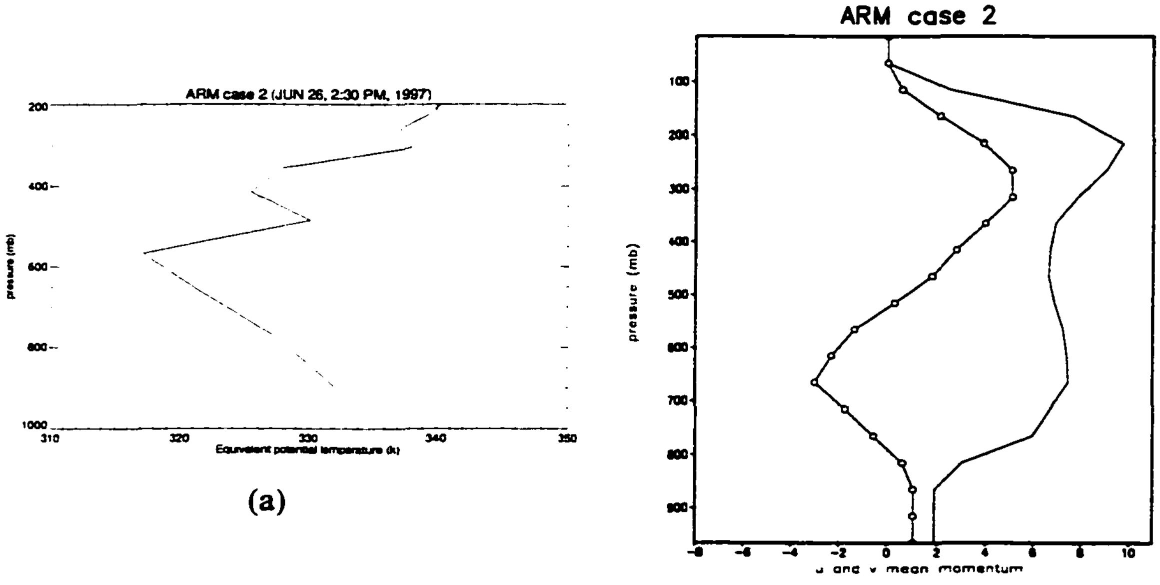

(a)

(b)

Figure 17: a) Environmental equivalent potential temperature sounding and (b) u (solid line) and v (line with open circles) mean wind for ARM case 2.

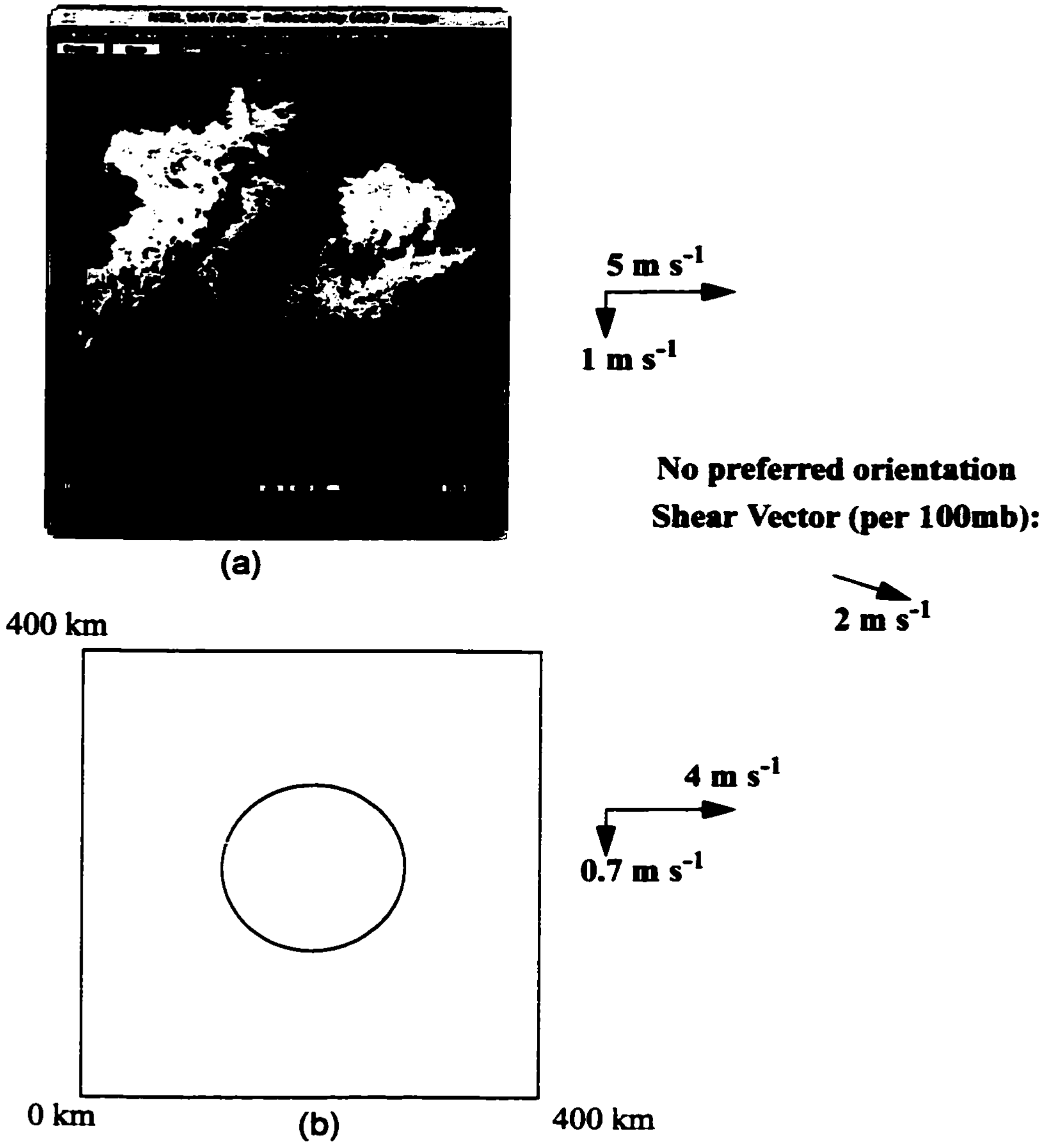

Figure 18: (a) Observed rain-band for June 26, 8:45 AM, 1997 (ARM Case 3), and (b) Organized cumulus cloud orientation from the theory, The model regards the organized clouds as a circular mass.

Fig. 18 (a) shows the organized clouds as observed by radar on June 26, 8:45 AM, 1997 (ARM Case 3). The size of the circular mass is estimated to be $150\ \text{km} \times 150\ \text{km}$. Fig. 18 (b) shows the clouds as predicted by the theory. The scale of the convective circle is about $109\ \text{km} \times 109\ \text{km}$. This is a very complex case. The left lobe and the right lobe of the cloud system are nonlinear MCSs. There is a small rain band lying in the north-east to south-west direction, which looks like a linear MCS in the center of the box. However, all of the clouds in the box are nonlinear MCSs according to the theory. Actually Case 3 occurred first, the organized clouds gradually became a weak linear MCS (ARM Case 2) in the afternoon. The phase speed from the model is 4 m s^{-1} in west-east direction, -0.7 m s^{-1} in south-north direction according to our theory. Compared to the radar data, the direction and speed are approximately right.

We use Fig. 19 to choose reference level. We find that the unstable layer is below 650 mb. This layer has a linear vertical wind structure. The largest vertical wind shear occurs between 700 mb and 900 mb. We choose 800 mb as the reference level since it is in the middle of the strongest wind shear and is unstable. In this level, the shear is about 2 m s^{-1} per 100 mb. The instability is close to our critical value at the reference level, so our theory regards the case as one with no preferred orientation. The vertical wind shear is also not strong enough to make a large difference between two arbitrary perpendicular directions. As a result, our theory regards it as a nonlinear MCS.

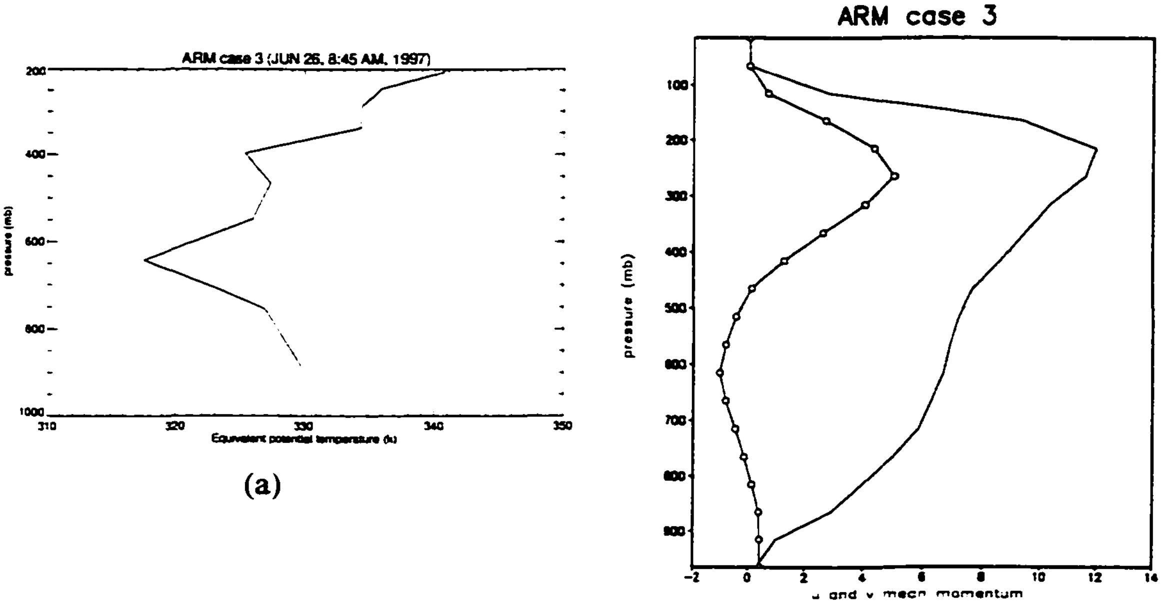

(a)

(b)

Figure 19: a) Environmental equivalent potential temperature sounding and (b) u (solid line) and v (line with open circles) mean wind for ARM case 3.

We also choose three cases from TOGA COARE IOPs to test our theory. The case of February 9, 1993 is a linear MCS case, which lasted from 9:30 AM to 12:15 PM. It is a typical squall line. The total rainfall is dominated by convective precipitation (Petersen et al. 1999). Fig. 20 (a) shows the organized clouds as observed by radar on February 9, 9:42 AM, 1992 (TOGA COARE Case 1). The size of the squall line can be calculated from the figure, which is about $18\ \mathrm{km} \times 156\ \mathrm{km}$. Fig. 20 (b) shows the clouds as predicted by the theory. According to our theory, the scale of the squall line is about $18\ \mathrm{km} \times 148\ \mathrm{km}$. The phase speed of the squall line is 9.5 m s^{-1} in north-east direction, and 0.6 m s^{-1} in east-south direction. Compared to the radar data, the direction and speed are approximately right. There are two squall lines in the observed image. However, they have the same

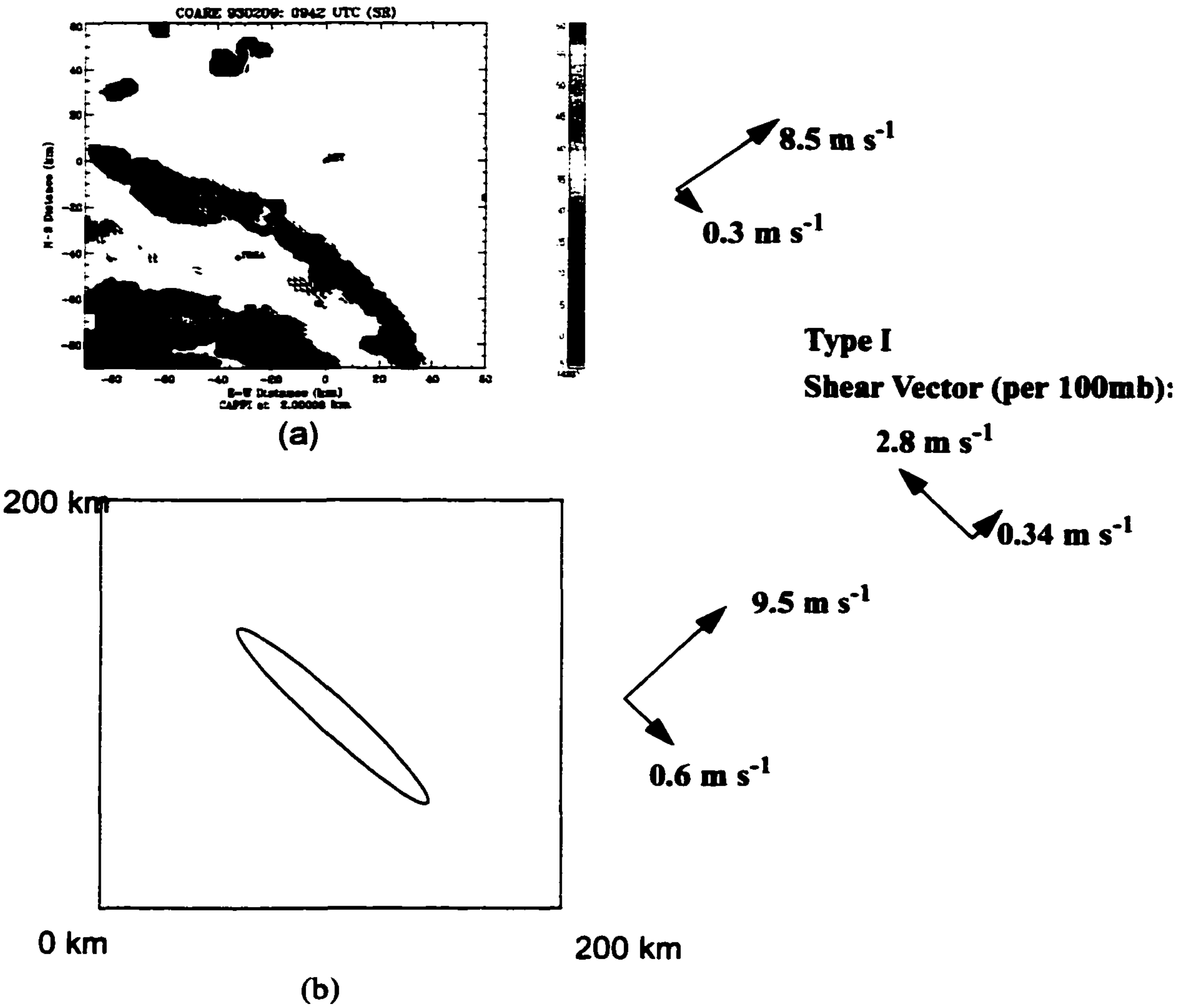

Figure 20: (a) Observed rain-band for February 9, 9:45 AM, 1993 (TOGA COARE Case 1), and (b) Organized cumulus cloud orientation from the theory, The model regards the organized clouds as a squall line whose long axis makes an angle of 45° with the x axis.

orientation. Our theory gives a good prediction. We choose the reference level using Fig. 21. The unstable level is below 600 mb. The largest level occurs between 600 mb and 800 mb. 700 mb is chosen as the reference level. At this level the instability is small, so this squall line belongs to our Type I.

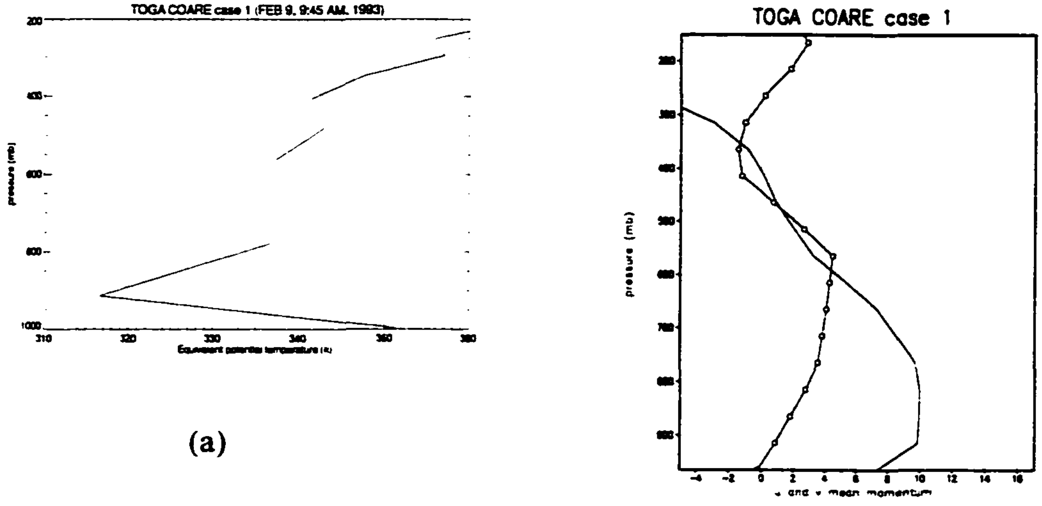

(a)

(b)

Figure 21: (a) Environmental equivalent potential temperature sounding and (b) u (solid line) and v (line with open circles) mean wind for TOGA COARE case 1.

Fig. 22 (a) shows the orientation and phase speed of the squall line as seen by radar on January 3, 7:00, 1993 (TOGA COARE Case 2). The size of the radar image is 400 km by 400 km. The resolution of the data is 2 km by 2 km. The size of the squall line is estimated to be $20\ \text{km} \times 250\ \text{km}$. Fig. 22 (b) shows the orientation and phase speed from the theory for that time. The scale of the convective ellipse is about $12.3\ \text{km} \times 269\ \text{km}$. The observed squall line is in the shape of an arch. Though the theory can only distinguish the line shape and circular shape, our theory predicts that the squall line has the shape of a line and lies in the north-west to south-east direction, which is approximately right. From our theory, the phase speed normal to the squall line is 12.4

m s^{-1} in north-east direction, and parallel to the line is 0.2 m s^{-1} south-east direction. Compared to the radar data, the line's speed and direction are approximately right.

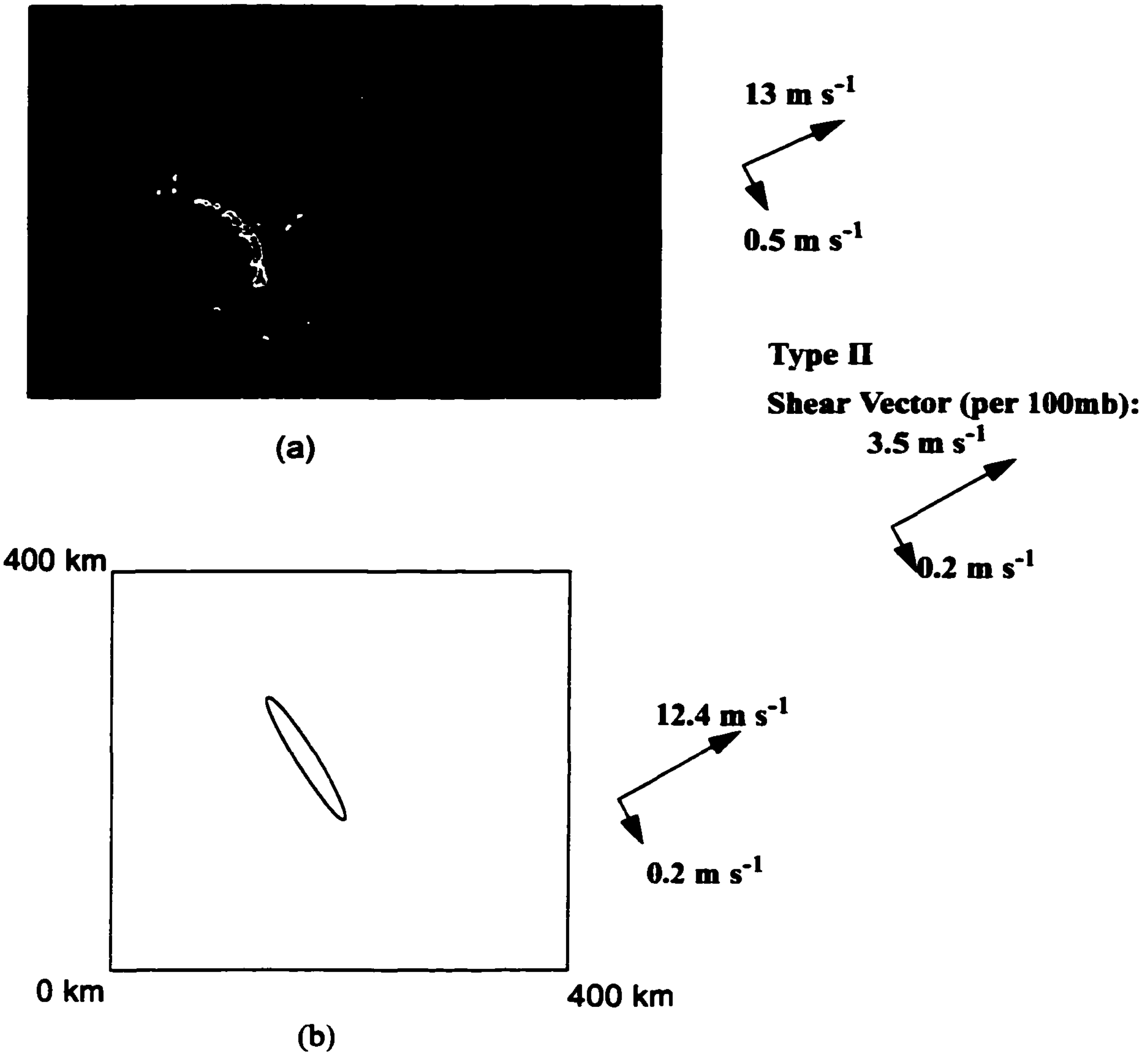

(a)

(b)

Figure 22: (a) Observed rain-band for January 3, 7:00 AM, 1993 (TOGA COARE Case 2), and (b) Organized cumulus cloud orientation from the theory, The model regards the organized clouds as a squall line whose long axis makes an angle of 60° with the x axis.

We choose reference level for this case using Fig. 23. The unstable level is below 600 mb. The vertical shear below this level has a very simple linear structure. The level of strongest shear is between 600 mb and 750 mb. It is also very unstable between these two levels, so 700 mb is chosen as the reference level. According our theory, this case belongs to Type II.

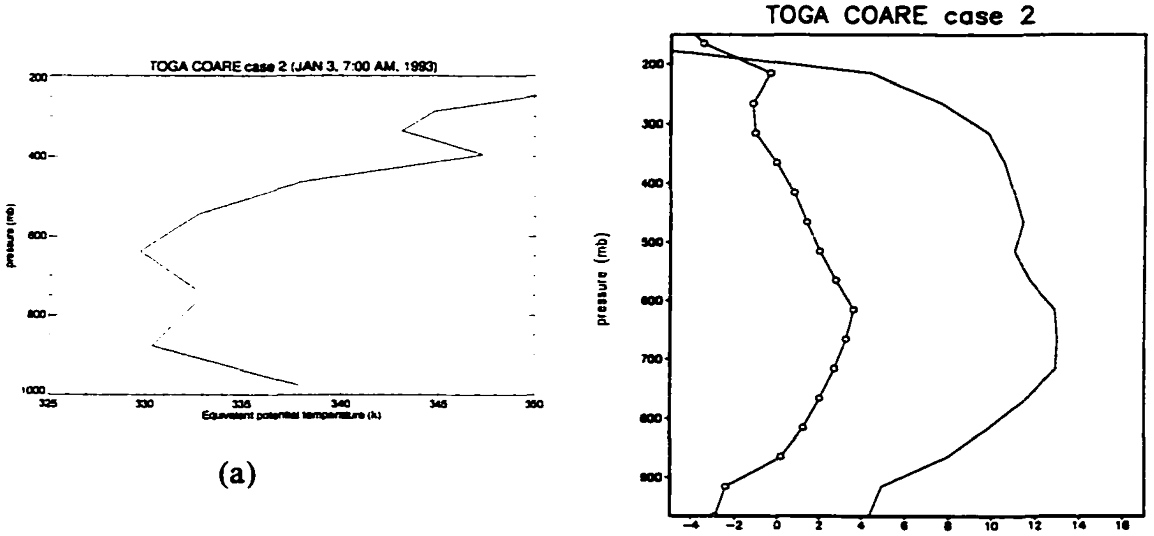

(a)

(b)

Figure 23: (a) Environmental equivalent potential temperature sounding and (b) u (solid line) and v (line with open circles) mean wind for TOGA COARE case 2.

Fig. 24 (a) shows the organized clouds as observed by radar on December 5, 9:00 PM, 1992 (TOGA COARE Case 3). The mesoscale system consists of individual convective cells, which are in a random state and do not have any linear structure. The size of the nonlinear MCS is estimated to be 150 km × 150 km. Fig. 24 (b) shows the clouds as predicted by the theory. The scale of the convective circle is about 108 km × 108 km. This is a nonlinear MCS. The phase speed from the model is 2.1 m s^{-1} in west-east

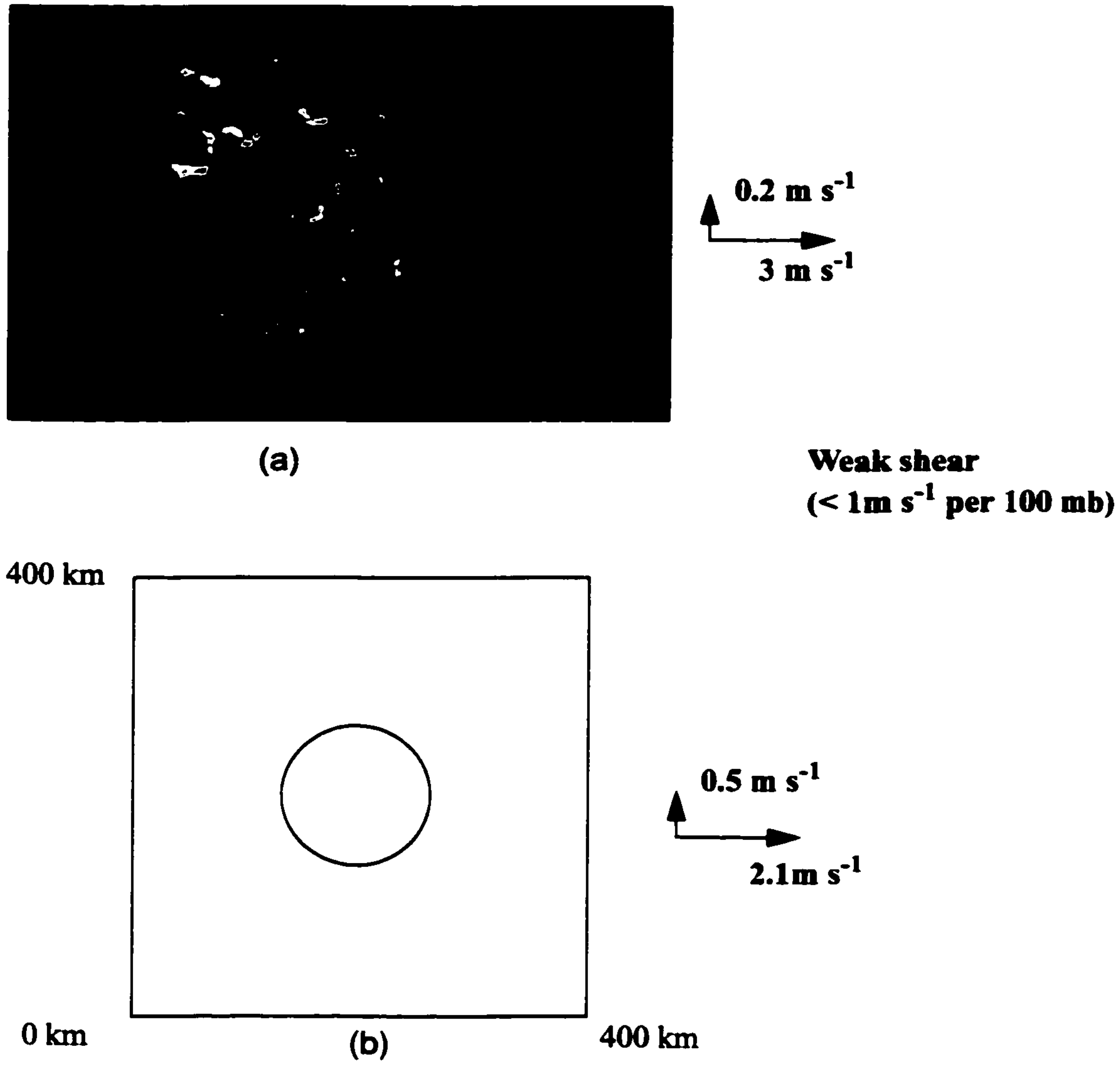

Figure 24: (a) Observed rain-band on December 5, 9:00 PM, 1992 (TOGA COARE Case 3), and (b) Organized cumulus cloud orientation from the theory, The model regards the organized clouds as a circular mass.

direction, 0.5 m s^{-1} in south-north direction according to our theory. Compared to the radar data, the direction and speed are approximately right.

We choose the reference level for this case using Fig. 25. The unstable levels are below 600 mb. The shears between 600 mb and 700 mb, and between 800 mb and 900 mb are large. The instability between 800 mb and 900 mb is larger than that between 600 mb and 700 mb. Therefore we choose the reference level to be between 800 mb and 900 mb. We choose 850 mb as the reference level. The shear at this level is less than 1 m s^{-1} per 100 mb, which is pretty weak. So this is a nonlinear MCS with weak shear.

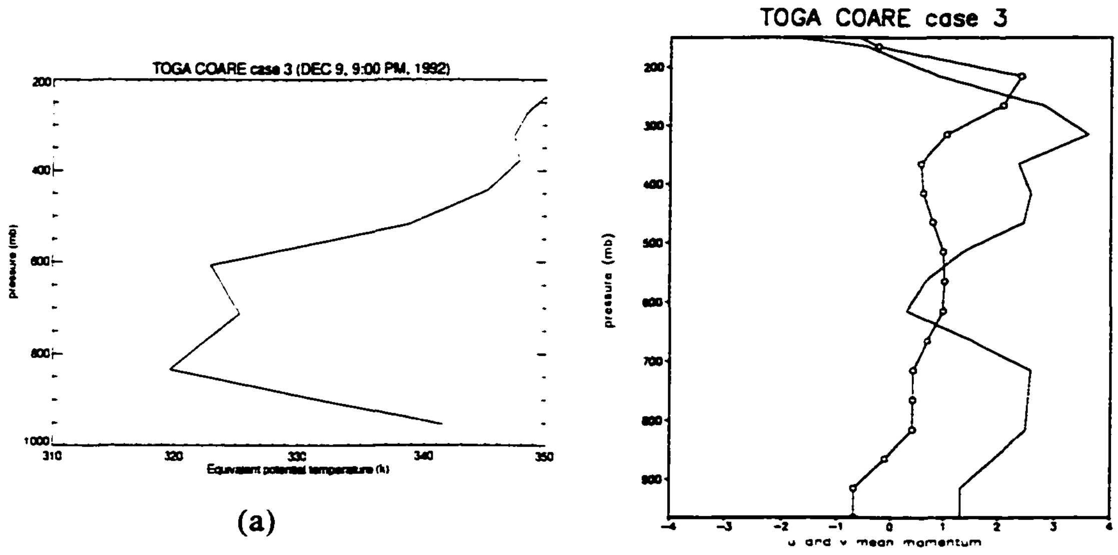

(a)

(b)

Figure 25: (a) Environmental equivalent potential temperature sounding and (b) u (solid line) and v (line with open circles) mean wind for TOGA COARE case 3.

V-A-2: The vertical momentum transport due to cumulus convection

V-A-2a: Nonlinear MCS case

The vertical transport of the horizontal momentum by nonlinear MCSs is very important because most of the organized clouds tend to be of this type. Fig. 26 shows the u and v wind components and their tendencies for the nonlinear MCS on June 26, 8:45 AM (ARM Case 3). Comparing the result from the MR and CR runs, we find that the effects of the perturbation pressure-gradient force tend to cancel the combined effects of detrainment and environmental subsidence in both directions. The effects of the perturbation pressure-gradient force are upgradient in the upper levels. This can be explained by (3.24) and (3.25) with $\theta = 0$:

$$-\sigma_c\left(\frac{1}{\rho}\cdot\frac{\partial p'}{\partial x}\right) = \frac{\nu_k}{\rho}\cdot\frac{\partial \bar{u}}{\partial z}M_c, \tag{5.4}$$

$$-\sigma_c\left(\frac{1}{\rho}\cdot\frac{\partial p'}{\partial y}\right) = \frac{\nu_l}{\rho}\cdot\frac{\partial \bar{v}}{\partial z}M_c. \tag{5.5}$$

The pressure-gradient force is positively proportional to the vertical wind-shear because ν_k, ν_l and M_c are all positive. In the upper layer, the vertical wind-shear is larger, so the acceleration is larger. The total transport is upgradient in both directions. We can see that

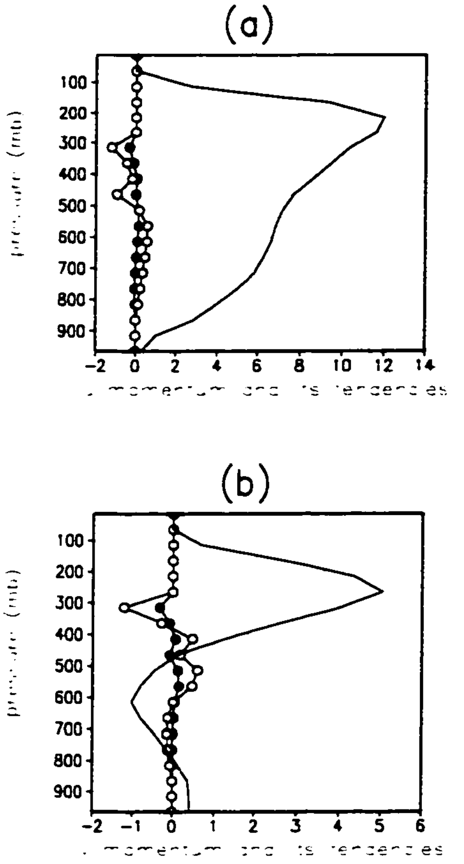

Figure 26: a), (b) are environmental u, v momentum ($m\ s^{-1}$, solid line) and their tendencies ($\times 10^5 m\ s^{-2}$, MR runs the line with closed circles, CR runs the line with open circles) on June 26, 8:45 AM, 1997 (ARM Case 3).

the tendencies tend to eliminate the vertical wind-shear. For example, the u momentum tends to decrease in the upper levels and increase in the lower levels. This can be explained when (5.4) and (5.5) are substituted into (2.5):

$$F_x = D_{cx}(u_{cx} - \bar{u}) + M_c\frac{\partial\bar{u}}{\partial z}(1 - \nu_k), \tag{5.6}$$

$$F_y = D_{cy}(v_{cy} - \bar{v}) + M_c\frac{\partial\bar{v}}{\partial z}(1 - \nu_l). \tag{5.7}$$

Because v_k and v_l are less than 1, u monotonically increases in z the direction, and v increases with z to about 600 mb, the contributions of the last two terms of (5.6) and (5.7) are positive. In the entrainment levels (low-levels, where $D_{cx} \approx 0$ and $D_{cy} \approx 0$), the air in the environment is accelerated; the air in the updraft is decelerated. In the detrainment-levels, the velocity of the air in the updraft is less than that of the environmental air, so the detrainment of the low-momentum air in the upper layer will decrease the shear (Wu and Yanai, 1994). If u decreases and then increases below the jet level, then the horizontal velocity of the air in the updraft can be larger than the environmental velocity. The detrainment of the higher momentum air will increase the shear. From (5.6) and (5.7), we also can see that the effects of the perturbation pressure-gradient force and vertical advection tend to cancel with each other, because v_x and v_y are always positive. For this case, vertical advection is dominant.

V-A-2b: Linear MCS case

We investigate two kinds of linear MCS cases here. In ARM Case 1, the line lies along the y axis, and in ARM Case 2, the line makes an angle with the y axis. Fig. 27 shows the u and v wind components and their tendencies for the linear MCS on July 15, 12:15 (ARM Case 1). Comparing the MR and CR runs, we find that the perturbation pressure-gradient force has almost no effect in the line-parallel direction (y direction), but has a strong effect in the line-normal direction (x direction). In the line-normal direction, the upgradient transport is caused mainly by the perturbation pressure-gradient force. The effects of both detrainment and environmental subsidence are downgradient in the line-normal direction. This is obvious from (5.6) and (5.7). In this case, $v_x > 1$ and $v_y \ll 1$, so the perturbation gradient force has a big effect in the x direction and almost no effect in the y direction. The upgradient momentum transport in the upper levels by the perturbation pressure-gradient force in the x direction is due to the same reason given before. The total transport (blue line) is downgradient in the y direction and upgradient in the x direction. Using (5.6) and (5.7), we find that the u momentum below the detrainment level is greater than that of the environment and v momentum is less than that of the environment, so detrainment will tend to strengthen the wind-shear in the u direction and weaken the wind-shear in the v direction at the upper levels.

Fig. 28 shows the u and v winds and their tendencies for the linear MCS on June 26, 14:30 (ARM Case 2). The line makes a small angle with the y direction. In the y direction. the total transport is downgradient. The perturbation pressure-gradient force tends to re-enforce the effects of the other two effects in the upper layer and to cancel the other two effects in the middle and lower layer. In the x direction, the total effect is to increase the wind in the upper layer and decrease the wind in the lower layer. The perturbation pressure-gradient force is the main factor causing the upgradient transport.

Because The momentum transport characteristics by linear MCSs and nonlinear MCSs during TOGA COARE IOPs are similar to those by linear MCSs and nonlinear MCSs during ARM IOPs, the figures are not shown here. In summary, the vertical

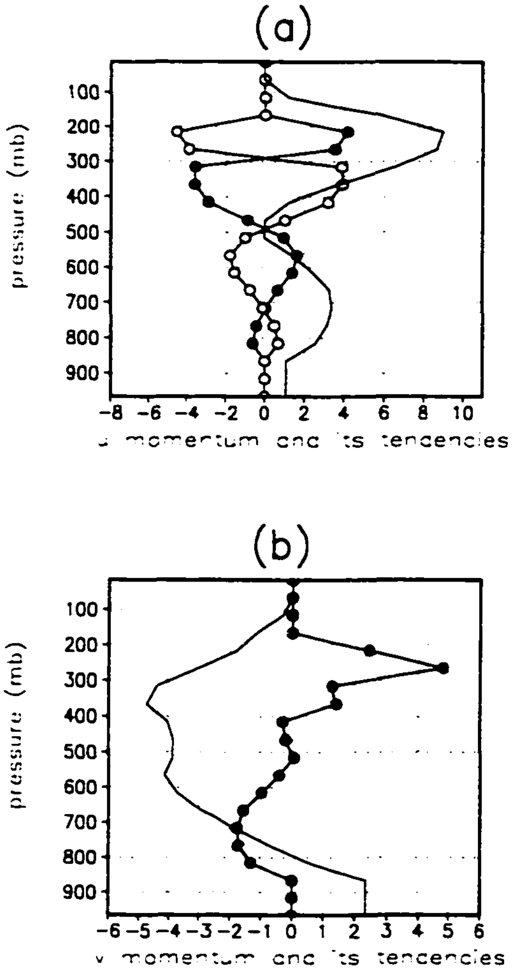

Figure 27: (a), (b) are environmental u, v momentum ($m\ s^{-1}$, solid line) and their tendencies ($\times 10^{5} m\ s^{-2}$, MR runs the line with closed circles, CR runs the line with open circles) on July 15, 12:15, 1997 (ARM Case 1)

momentum transport associated with the perturbation pressure-gradient force tends to be upgradient in both directions for nonlinear MCSs, and in the line-normal direction for linear MCSs. This is consistent with the conclusions of Moncrieff (1992) and Wu and Yanai (1994).

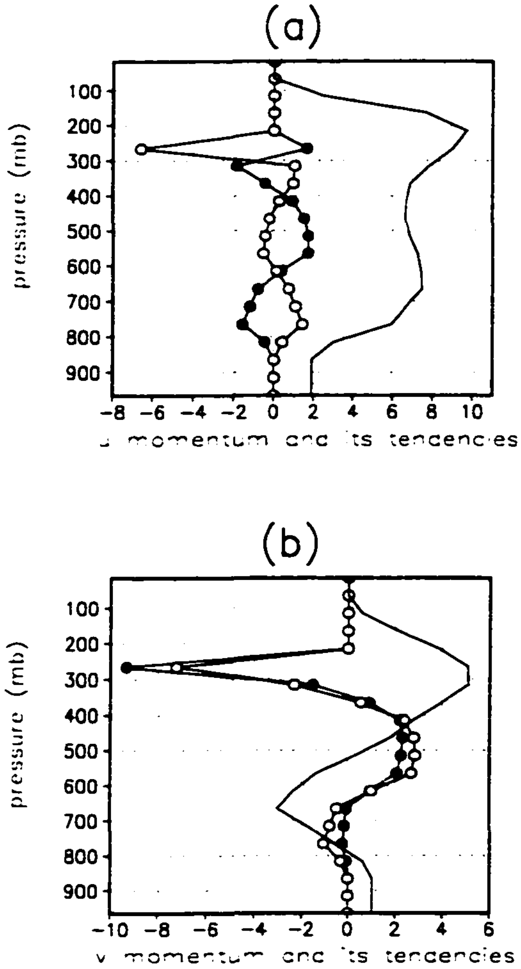

Figure 28: **(a), (b) are environmental u, v momentum ($m\ s^{-1}$, solid line) and their tendencies ($\times 10^5 m\ s^{-2}$, MR runs the line with closed circles, CR runs the line with open circles) on June 26, 14:30, 1997 (ARM Case 2)**

The total momentum transport is downgradient in both directions for the nonlinear MCSs. Stevens 1979, Tollerud and Esbensen 1983, LeMone et al. 1984, and Sui and Yanai 1986 reported downgradient convective momentum transport for nonlinear MCSs. For linear MCSs, the total momentum transport tends to be upgradient in the line-normal direction. Moncrieff and Green 1972, Tollerud and Esbensen 1983, Lafore et al. 1988, LeMone and Jorgensen 1991, and Gallus and Johnson 1992 reported upgradient momentum transport associated with cumulus clouds for this case. It tends to be downgradient in the line-parallel direction. These results are consistent with the studies of Asai (1970), LeMone and Jorgensen (1991) and Wu and Yanai (1994).

The effects of the perturbation pressure-gradient force and the effects by vertical advection and detrainment tend to cancel with each other. This result is consistent with the study of Wu and Yanai (1994).

V-A-3: The effects of shear production in the CKE equation

Because the updraft horizontal velocity is known, the shear-production term can be included in CKE equation:

$$-\rho\overline{u'w'}\frac{\partial\bar{u}}{\partial z}-\rho\overline{v'w'}\frac{\partial\bar{v}}{\partial z} = -M_c\left[(u_c-\bar{u})\frac{\partial\bar{u}}{\partial z}+(v_c-\bar{v})\frac{\partial\bar{v}}{\partial z}\right]. \qquad (5.8)$$

Fig. 29 (a) and (b) show the contribution of CKE due to buoyancy and shear production terms respectively. The lines with plus signs are for the simulation with shear production terms added. The solid lines are for the simulation without shear production in the CKE equation, but the line with plus signs appears in (b) for the purpose of comparison. We see that shear production can be positive or negative, depending on the vertical wind-shear and the velocity difference between the clouds and the environment. The average negative shear production rate is about $-2\ \mathrm{J\ m^{-2}\ s^{-1}}$. The average positive shear production rate is about 2 $\mathrm{J\,m^{-2}\,s^{-1}}$. The average positive buoyancy production rate is about 300 $\mathrm{J\,m^{-2}\,s^{-1}}$. So the shear production rate is about 1% of buoyancy production rate, i.e. two orders of magnitude smaller.

We also plot the cumulus precipitation rate and the total precipitation rate for this period in Fig. 30. The precipitation rates are averaged values for the nine simulations with small changes of the initial conditions, so that the influences of the initial conditions are eliminated (Hack, 2000). Both Fig. 29 a and b show little difference between the simulations with and without shear production. This is because shear-production is not always uniformly positive or negative through the whole convective event (Fig. 29 b), and it is very small, so its influence is very small.

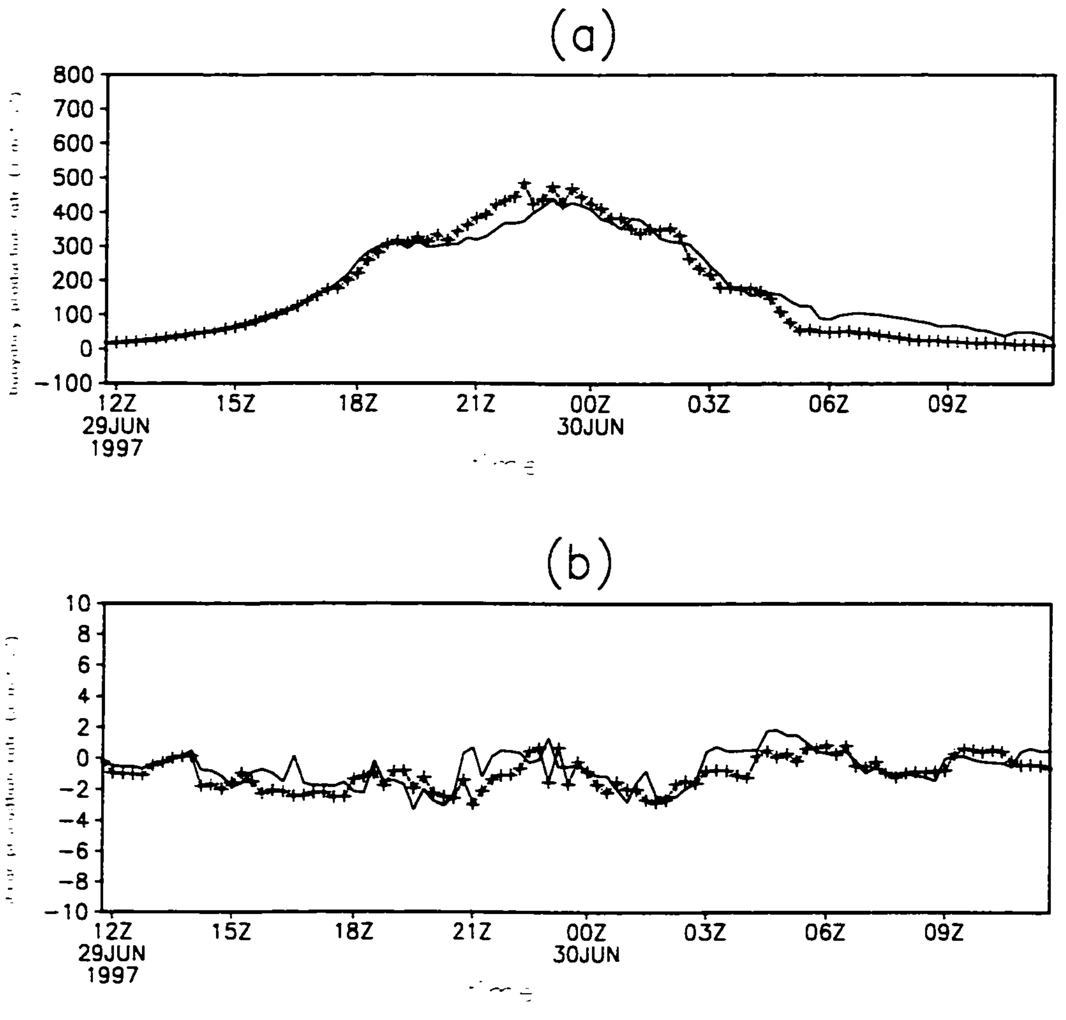

Figure 29: (a) Buoyancy production rate and (b) shear production rate for CKE equation. The line with plus signs is for CKE runs, the solid line MR runs.

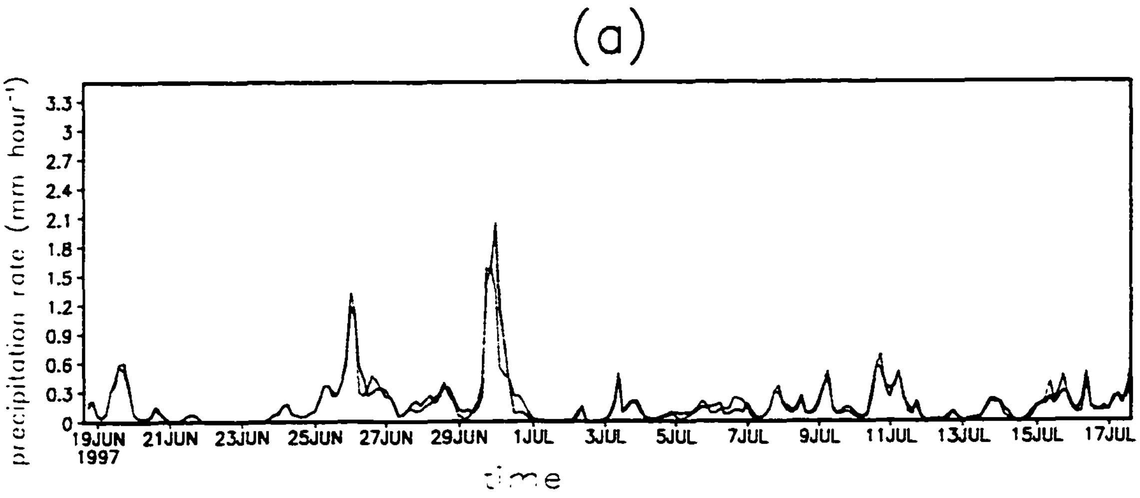

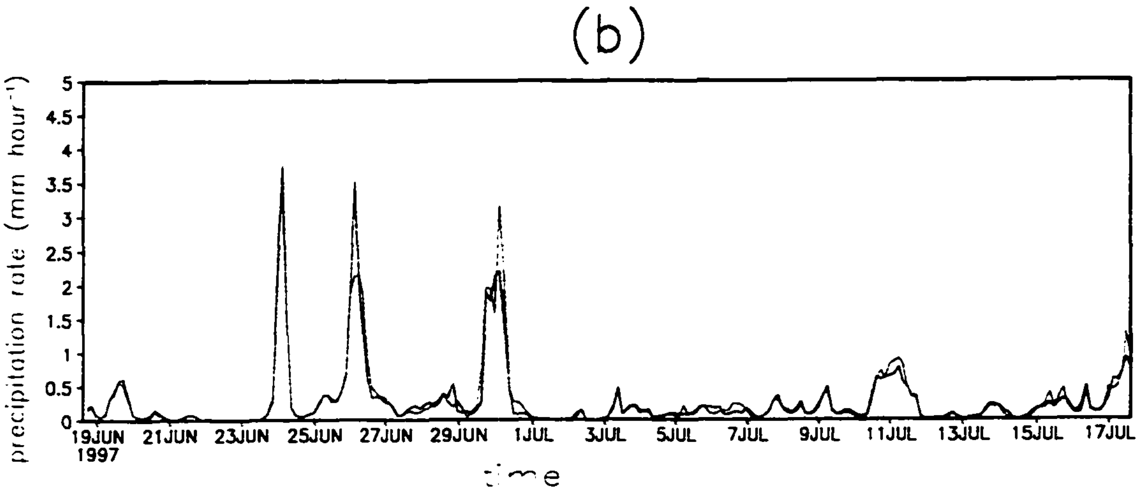

Figure 30: (a) precipitation rate by convective clouds and (b) total precipitation rate. Red line is for CKE runs, green line MR runs.

Chapter VI: Summary and discussion

In this study, a parameterization of cumulus momentum transport has been proposed. The most important feature of this scheme is that the orientation, aspect ratio, and phase speed of organized convection are determined. Another important feature is the inclusion of the perturbation pressure-gradient force induced by interactions between the updraft and the environmental wind.

By comparing the predicted orientation, aspect ratio and phase speed of organized convection with those observed by radar, we find that our theory gives the right answers. According to our theory, the orientation of a squall line can make any angle with the vertical wind-shear.

The effects of convective-scale momentum transport have also been studied. The vertical momentum redistribution is systematically different between linear and nonlinear MCSs. For non-linear MCSs, the total momentum transport tends to be downgradient, but one of the two components (u or v) can be upgradient if the environmental wind profile has a certain shape. For linear MCSs, line-normal vertical momentum transport tends to be upgradient, while line-parallel transport tends to be downgradient.

The momentum transport due to the perturbation pressure-gradient force has effects not only at higher levels, but also at lower levels. It tends to make the transport upgradient and tends to cancel with vertical momentum advection and detrainment effects.

We find that the shear production term has little effect in the CKE equation.

Compared with Wu and Yanai's (1994) scheme, our scheme is more complete because we have figured out a way to calculate the orientation of the organized cumulus clouds. In addition, our theory of the perturbation pressure-gradient force extends that of Wu and Yanai. The organized cumulus clouds in our theory are seen as entities embedded inside a mesoscale system, so the momentum transport mechanism of the cumulus clouds is easy to understand. We also consider the nonlinear effects on the perturbation pressure-gradient force, which are significant in the vertical direction. Further discussion will be given elsewhere.

When $\frac{v_k}{\rho}$ and $\frac{v_l}{\rho}$ are constants in (3.9) and (3.10), our scheme becomes Kershaw et al.'s (1997a, 1997b) scheme. So their scheme is a special case of our scheme.

Our theory can easily be subjected to tests using observations. Although we have used GATE, ARM, EMEX, SCSMEX, and TOGA COARE cases to test the theory, more tests are necessary. Our criterion to distinguish line parallel and line normal linear MCSs is the instability near reference level. A reference level must satisfy two conditions. Even with weak instability at the reference level, there can be strong instability in the other layers, so the CAPE and growth rate for Type I can still be larger. That is the reason why we can not distinguish Type I and Type II using CAPE and growth rate as criteria. CAPE and growth rate must be pretty large for Type II MCSs, but they are not necessary small for Type I. Houz (1990) reported strong Type II squall lines with leading line/trailing-stratiform structure and weak Type I squall lines.

Using the methods described above, we can obtain the velocity of convective systems, which is important for the physical processes in GCMs. For example, a slowly moving convective system tends to produce heavy local rain and long-lasting local cloud.

Our scheme also diagnostically determines the vertical velocity of the updraft air, which is important for the parameterizations of the microphysical processes inside cumulus clouds.

Because our parameterization predicts the momentum of the updraft, The tilting angle of the updraft can be obtained without any iterative method. The rain water loading, vertical wind-shear, and the phase speed of the mesoscale systems are used to determine the momentum of the updraft. The parameterization of the downdraft for GCMs is simplified as a result (Cheng and Arakawa, 1997). However, the tilted updraft can occur without shear due to the dragging of rain water and the moving of new produced convective cells. Our approach can not predict the tilting angle of this kind of updraft. It is a challenging work in the future.

However, many important, interesting and challenging questions remain. What are the effects of the downdrafts and the mesoscale system on the vertical momentum transport? The formulae ((3.24) and (3.25)) of the perturbation pressure-gradient force for the mesoscale system is the same as that of updraft. However, the area of the mesoscale system is much larger than those of the cumulus clouds. The mass flux of the mesoscale system is also much smaller that those of cumulus clouds. Because the vertical profile of downdraft vertical velocity is not a bell shape, we expect a different perturbation pressure-gradient force formulae. We also expect downdraft can bring higher momentum air from upper troposphere to lower troposphere. The updraft, downdraft and the mesoscale system also interact with each other. The total momentum transport inside a grid box will not be the simple sum of the transport by these three. Mesoscale upward momentum transport can be made strong by updraft upward transport and weak by downdraft downward transport. Because updraft and downdraft are organized by mesoscale system, their vertical momentum transports will be highly influenced by mesoscale systems.

There is conditional symmetric instability (CSI) in both mid-latitude cyclones and tropical cyclones. It leads to rainbands making a small angle with temperature contours. The length scale along the bands can be as large as hundreds of kilometers, while the length scale perpendicular to the rainband is less than one hundred kilometers. The parcel-trajectory of CSI is more slantwise than that of cumulus clouds. The trajectory of an updraft and downdraft parcel has great influence on the trajectory of an CSI parcel. For example, Chan and Thorpe's (1993) CSI parameterization need the trajectory of an updraft and downdraft parcel as an important parameter which must be input to the scheme. Our theory provides good background (updraft tilting angle and momentum forecast) for the prediction of trajectory for updraft and downdraft.

Convective rainbands can occur in the atmosphere with neutral stability (according our theory, Type I linear MCS should occur). This is because the conversion from large-scale kinetic energy to convective kinetic energy becomes possible when CSI occurs. Emanuel (1983) show the Slantwise Convective Available Potential Energy (SCAPE) is

$$SCAPE = \int_0^H \left\{ \frac{g}{\theta_{v0}} \Delta \left(\theta_v + \frac{1}{2} \frac{f}{\eta(z))} \frac{d}{dz} [(v - v_0)^2] \right) \right\} dz \ , \tag{6.1}$$

where H is the highest height that the parcel can reach, θ_v is the virtual potential temperature, η and f are absolute and planetary vorticity and v is the parcel's velocity. Subscript 0 represents parcel. The first term on right-hand side of (6.1) is CAPE. The second term is the contribution from the kinetic energy, which may be large enough to compensate the negative value of CAPE. The organization of convective clouds can be influenced by CSI. Tomas and Webster (1997) reported that when there are CSI associating with rising motion, deep convection and vertical circulation extend throughout the troposphere. They argued that the reason why off-equator convection is deeper than near-equatorial convection is due to CSI is active there. However, more work is needed to be done on the interaction between CSI and convective clouds.

Parameterization of CSI in a GCM is a challenging and interesting work. We need to consider mesoscale system, CSI and convection at the same time. Their interaction will be quite complex. However, this work is also rewarding. The simulated convection and clouds will be more realistic. Nordeng (1987) included a Kuo-type parameterization of CSI in an operational model with 50 km horizontal resolution. The precipitation can be found in bands. The simulated momentum structures (Lindstrom and Nordeng, 1992) are similar to those observed. The effects of CSI are to produce more convective precipitation, and to strengthen the grid-scale updraft. The rainfall prediction in their model is much more accurate.

APPENDIX

Derivation of the formula of the pressure-gradient force

Deriving (3.9)-(3.11), (3.13)-(3.15), (3.17)-(3.19), (3.21)-(3.23) is a purely mathematical process. I derive (3.9) here as an example. The derivations of the rest are even easier than this one.

From (3.8):

$$-\frac{1}{\rho}\frac{\partial p'_{shear}}{\partial x} = -\frac{2}{(k^2+l^2+m^2)}\cdot \left[-\frac{\partial \bar{u}}{\partial z}k^2\left(\sin(kx')\sin(ly') + \frac{\partial \bar{v}}{\partial z}kl\cos(kx')\cos(ly')\right)\right]\hat{w}\sin(mz) \quad . \tag{A.1}$$

For the following ellipse:

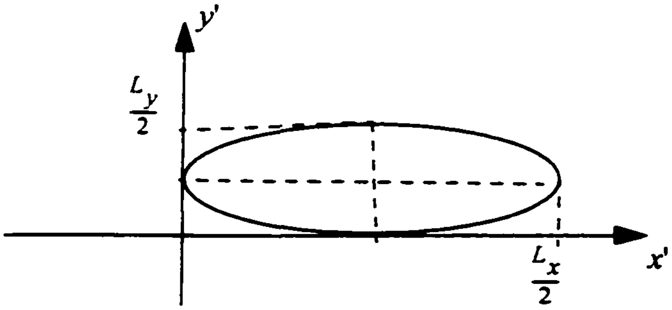

Figure 31: Shape of the organized convective clouds (for integration)

Area s is:

(A.2) $$s = \frac{\pi L_x L_y}{16}.$$

The following relationships for wave number k and l exist:

(A.3) $$k = \frac{2\pi}{L_x},$$

(A.4) $$l = \frac{2\pi}{L_y}.$$

We have:

(A.5) $$-\sigma\left(\frac{1}{\rho}\cdot\frac{\partial p'}{\partial x'}\right)_{\sigma,\,shear} = \int_{(s)}\frac{1}{\rho}\cdot\frac{\partial p'}{\partial x'}dx'dy' = \frac{2\hat{w}\sin(mz)}{(k^2+l^2+m^2)}\left[\frac{\partial\bar{u}}{\partial z}k^2\int_{(s)}\sin(kx')\sin(ly')dx'dy' - \frac{\partial\bar{v}}{\partial z}kl\int_{(s)}\cos(kx')\cos(ly')dx'dy'\right].$$

The equation of this ellipse is:

(A.6) $$\frac{\left(x'-\frac{L_x}{4}\right)^2}{\left(\frac{L_x}{4}\right)^2}+\frac{\left(y'-\frac{L_y}{4}\right)^2}{\left(\frac{L_y}{4}\right)^2} = 1.$$

Both numerator and denominator of the first term on right-hand side are divided by L_x^2 and those of the second term on right-hand side is divided by L_y^2:

$$\text{(A.7)} \qquad \frac{\left(\frac{x'}{L_x}-\frac{1}{4}\right)^2}{\left(\frac{1}{4}\right)^2}+\frac{\left(\frac{y'}{L_y}-\frac{1}{4}\right)^2}{\left(\frac{1}{4}\right)^2} = 1 .$$

Using (A.3) and (A.4):

$$\text{(A.8)} \qquad \frac{\left(\frac{kx'}{2\pi}-\frac{1}{4}\right)^2}{\left(\frac{1}{4}\right)^2}+\frac{\left(\frac{ly'}{2\pi}-\frac{1}{4}\right)^2}{\left(\frac{1}{4}\right)^2} = 1 .$$

Both numerator and denominator of the terms on right-hand side multiple by 16:

$$\text{(A.9)} \qquad \left(\frac{2kx'}{\pi}-1\right)^2+\left(\frac{2ly'}{\pi}-1\right)^2 = 1 .$$

We have got:

$$\text{(A.10)} \qquad ly' = \frac{\pi}{2}\left[1 \pm \sqrt{1-\left(\frac{2kx'}{\pi}-1\right)^2}\right] .$$

Now solve the two integrations on right-hand side of (A.5)

$$\text{(A.11)} \qquad \int_{(s)} \sin(kx')\sin(ly')dx'dy' = \int_0^{\pi} \sin(kx') \int_{\frac{\pi}{2}\left[1-\sqrt{1-\left(\frac{2kx'}{\pi}-1\right)^2}\right]}^{\frac{\pi}{2}\left[1+\sqrt{1-\left(\frac{2kx'}{\pi}-1\right)^2}\right]} \sin(ly')dx'dy' .$$

Let $X = kx'$ and $Y = ky'$:

$$\text{(A.12)} \quad \int\limits_{(s)} \sin(kx')\sin(ly')dx'dy' = \int\limits_{0}^{\pi} \sin X\left\{\cos\left(\frac{\pi}{2}\left[1+\sqrt{1-\left(\frac{2X}{\pi}-1\right)^2}\right]\right) - \cos\left(\frac{\pi}{2}\left[1-\sqrt{1-\left(\frac{2X}{\pi}-1\right)^2}\right]\right)\right\}dXdY \ .$$

Integrate (A.12) using numerical method:

$$\text{(A.13)} \quad \int\limits_{(s)} \sin(kx')\sin(ly')dx'dy' = \frac{3.86}{kl}.$$

Using the same method, we get

$$\text{(A.14)} \quad \int\limits_{(s)} \cos(kx')\cos(ly')dx'dy' = \frac{1.8\times10^{-8}}{kl}.$$

Compare (A.13) and (A.14), because the value of the second integration is too small, we neglect it. So we have

$$\text{(A.15)} \quad -\sigma\left(\frac{1}{\rho}\cdot\frac{\partial p'}{\partial x'}\right)_{\sigma,\,shear} = \frac{2k^2}{(k^2+l^2+m^2)}\frac{\partial\bar{u}}{\partial z}\left(\frac{3.86}{kl}\right)\hat{w}\sin(mz).$$

From the definition of $\overline{w_s}$:

$$\text{(A.16)} \quad \overline{w_s} = \frac{\hat{w}\sin(mz)}{s}\int\limits_{(s)} \sin(kx')\sin(ly')dx'dy'.$$

Using (A.13),

(A.17) $$\overline{w_s} = \frac{\hat{w}\sin(mz)}{\frac{\pi L_x L_y}{16}}\frac{3.86}{kl} = \frac{4 \times 3.86}{\pi^3}\hat{w}\sin(mz).$$

Therefore,

$$-\sigma\left(\frac{1}{\rho}\cdot\frac{\partial p'}{\partial x'}\right)_{\sigma,\,shear} = \frac{\nu_k}{\rho}\frac{\partial\bar{u}}{\partial z}\left(\rho\frac{3.86 L_x L_y}{4\pi^2}\right)\hat{w}\sin(mz)$$

$$= \frac{\nu_k}{\rho}\frac{\partial\bar{u}}{\partial z}\rho\left(\frac{4 \times 3.86}{\pi^3}\hat{w}\sin(mz)\right)\frac{\pi L_x L_y}{16} = \frac{\nu_k}{\rho}\frac{\partial\bar{u}}{\partial z}\rho\overline{w_s}s = \frac{\nu_k}{\rho}\frac{\partial\bar{u}}{\partial z}M \quad ,$$

where $M = \rho\overline{w_s}s$ is the convection mass flux.

REFERENCES

Alexander, G. D., and G. S. Young, 1992: The relationship between EMEX mesoscale precipitation feature properties and their environmental characteristics. *Mon. Wea. Rev.*, **120**, 554-564.

Arakawa, A., and W. H. Schubert, 1974: The interaction of a cumulus cloud ensemble with the large-scale environment, Part I. *J. Atmos. Sci.*,**31**,674-701.

--------------, Y. Mintz, A. Katayama, J. -W. Kim, W. Schubert, T. Tokioka, M. Schlesinger, W. Chao, D. A. Randall and S. Lord, 1972: The UCLA atmospheric General Circulation Model, *Notes Distributed at the workshop*, 25 March - 4 April 1974, Department of Meteorology, University of California, Los Angeles, California 90024.

Asai, T., 1970: Three-dimensional features of thermal convection in a plane Couette flow. *J. Meteor. Soc. Japan*, **48**, 18-29.

Asai, T., 1970: Stability of a plane parallel flow with variable vertical shear and unstable stratification. *J. Meteor. Soc. Japan*, **48**, 129-138.

Asai, T., 1972: Thermal instability of a shear flow turning the direction with height. *J. Meteor. Soc. Japan*, **50**, 525-531.

Barnes, G.M., and K. Sieckman, 1984: The environment of fast- and slow-moving tropical mesoscale convective cloud lines. *Mon. Wea. Rev.*, **112**, 1782-1794.

Barnes, S. L., 1964: A technique for maximizing details in numerical weather map analysis. *J. Appl. Meteor.*, **3**, 396-409.

Bechtold, P., et al., J.-L. Redelsperger, I. Beau, M. Blackburn, S. Brinkop, J.-Y. Grandpeix, A. Grant, D. Gregory, F. Guichard, C. Hoff, and E. Ioannidou, 2000: A GCSS model intercomparison for a tropical squall line observed during TOGA-COARE, part II, Intercomparison of SCMs with CRM, *Q. J. R. Meteorol. Soc.*, **126**, 865-888.

Betts, A.K., 1976: The thermodynamic transformation of the tropical subcloud layer by precipitation and downdrafts. *J.Atmos.Sci.*, **33**, 1008-1020.

Bluestein, H. B., and M.H. Jain, 1985: Formation of mesoscale lines of precipitation: Severe squall lines in Oklahoma during the spring. *J.Atmos.Sci.*,**42**,1711-1732.

-----------------, G.T. Marx and M.H. Jain, 1987: Formation of mesoscale lines of precipitation: Non-severe squall lines in Oklahoma during the spring. *Mon. Wea. Rev.*, **115**,2719-2727.

Carr, M. T. and C. S. Bretherton, 2001: Convective momentum transport over the tropical pacific: budget estimates. *J. Atoms. Sci.*, **58**, 1673-1693.

Chan, C. S. and A. J., Thorpe, 1993: A parameterization scheme for symmetric instability: tests for an idealized flow.

Cheng, M.-D., 1989a: Effects of downdrafts and mesoscale convective organization on the heat and moisture budgets of tropical cloud cluster. Part I: A diagnostic cumulus ensemble model. *J. Atoms. Sci.*, **46**, 1517-1538.

------, -------, A. Arakawa, 1997: Inclusion of rainwater budget and convective downdrafts in the Arakawa-Schubert cumulus parameterization. *J. Atoms. Sci.*, **54**, 1359-1379.

Ding, P., and D. A. Randall, 1998: A cumulus parameterization with multiple cloud-base levels. *J. Geophys. Res.*,**103**,11341-11354.

Emanuel, K. A., 1983: On assessing local conditional symmetric instability from atmospheric soundings. *Mon. Wea. Rev.*, **111**, 2016-2033.

Fowler, L. D., D. A. Randall, and S. A. Rutledge, 1996: Liquid and ice cloud microphysics in the CSU General Circulation Model. Part I: Model description and simulated microphysical processes. *J. Climate*, **9**, 489-529.

Fowler, L. D., and D. A. Randall, 1996 a: Liquid and ice cloud microphysics in the CSU General Circulation Model. Part II: Simulation of the earth's radiation budget. *J. Climate*, **9**, 530-560.

Fowler, L. D., and D. A. Randall, 1996 b: Liquid and ice cloud microphysics in the CSU General Circulation Model. Part III: Sensitivity tests. *J. Climate*, **9**, 561-586.

Frank, W.M.,1978: The life cycle of GATE convective systems. *J.Atmos.Sci.*, **35**,1256-1264.

Gallus, W. A., Jr., and R. H. Johnson, 1992: The momentum budget of an intense midlatitude squall line. *J. Atmos. Sci.*, **49**, 422-450.

Gregory, D., R. Kershaw, and P. M. Inness, 1997b: Parameterization of momentum transport by convection. Part II: Tests in single column model and general circulation models. *Quart. J. Roy. Meteor. Soc.*, **123**, 1153-1183.

Hack, J. J. and J. A., Pedretti, 2000: Assessment of solution uncertainties in single-column modeling frameworks. *J. Climate*, **13**, 352-365.

Hane, C., E., and P. S. Ray, 1985: pressure and buoyancy fields derived from Doppler radar data in a tornadic thunderstorm. *J. Atmos. Sci.*, **42**, 18-35.

Harshvardhan, R. Davies, D. A. Randall, and T. G. Corsetti, 1987: A fast radiation parameterization for atmospheric circulation models. *J. Geophys. Res.*, **92**, 1009-1016.

Holton, J.R., 1973: A one-dimensional cumulus model including pressure perturbations. *Mon. Wea. Rev.*, **101**, 201-205.

Houz, R. A., B. F., Smull and P., Dodge, 1990: Mesoscale organization of springtime rainstorms in Oklahoma. *Mon. Wea. Rev.*, **118**,613-654.

Johnson, R.H., and P. J. Hamilton, 1988: The relationship of surface pressure features to the precipitation and airflow structure of an intense midlatitude squall line. *Mon. Wea. Rev.*, **116**,1444-1472.

-----------------, and T.D. Keenan, 2001: Organization of oceanic convection during the onset of the 1998 East Asian summer monsoon. *Preprints, 30th International Conference on Radar Meteorology, Amer. Meteor. Soc.*, Munich, Germany.

Jorgensen, D. P., M. A, LeMone, and *B.* J.-D. Jou, 1991: Precipitation and kinematic structure Of an Oceanic mesoscale convective system. Part 1: Convective line structure. *Mon. Wea. Rev.*, **119**, *2*608-2637.

Kuo, H. L., 1963: Perturbations of plane Couette flow in stratified fluid and origin of cloud streets. *Phys. of Fluids*, **6**, 195-211.

Kershaw, R. and D. Gregory,1997a: Parameterization of momentum transport by convection. part I. Theory and cloud modelling results. *Quart. J. Roy Meteor. Soc.*, **123**, 1133-1151.

Lafore, J.-P., J-L. Redelsperger, and G. Jaubert, 1988: Comparison between a three-dimensional simulation and Doppler radar data of a tropical squall line: Transports of mass, momentum and moisture. *J. Atmos. Sci.*, **45**, 3483-3500.

Leach, M. J., J. Yio, and R. T. Cederwall, 1996: Estimation of Errors in Objectively Analyzed fields and sensitivity to number and spacing of stations. *Proceedings of the sixth Annual Atmospheric Radiation Measurement (ARM) Science Team Meeting,* San Antonio, TX., DOE CONF-9603149, 149-151. (Available from the U. S. Dept. of commerce, Technology Administration, National Technical INformation SErvice, Springfield, VA 22161, (703) 487-4650.)

Leach, M. J., J. Yio, and R. T. Cederwall, 1997: Improvements in the LLNL objective analysis scheme for deriving forcing fields for Single-Column Models using ARM data. *Proceedings of the sixth Annual Atmospheric Radiation Measurement (ARM) Science Team Meeting*, San Antonio, TX., DOE CONF-9603149, 149-151. (Available from the U. S. Dept. of commerce, Technology Administration, National Technical Information SErvice, Springfield, VA 22161, (703) 487-4650.)

LeMone, M. A., and M. W. Moncrieff, 1994: Momentum and mass transport by convective bands: Comparisons of highly idealized dynamic models to observations. *J. Atmos. Sci.*, **51**, 281-305.

--, 1993: Momentum transport by convective bands: comparisons of highly idealized dynamical models to observations. The representation of cumulus convection in numerical models. *Meteorological Monographs*, **24**, 75-92.

----------------, and D. P. Jorgensen, 1991: Precipitation and kinematic structure of an oceanic mesoscale convective system. Part 11: Momentum transport and generation. *Mon. Wea. Rev.*, **119**, 2639-2653.

----------------, G. M. Barnes, and E. J. Zipser, 1984: Momentum flux by lines of cumulonimbus over the tropical oceans. *J. Atmos. Sci.*, **41**,1914-1932.

-----------------, G. M. Barnes, J.C. Fankhauser, and L. F. Tarleton, 1988: Perturbation pressure fields measured by aircraft around the cloud base updraft of deep convective clouds. *Mon. Wea. Rev.*, **116**, 313-327.

----------------, E. J. Zipser and S. B. Trier,1998: The role of environmental shear and thermodynamic conditions in determining the structure and evolution of mesoscale convective systems during TOGA COARE. *J. Atmos. Sci.*, **55**, 3493-3518.

Lin, X. and R. H. Johnson, 1996 a: Kinematic and thermodynamic characteristics of the flow over the western pacific warm pool during TOGA COARE. *J. Atmos. Sci.*, **53**, 695-715.

Lin, X. and R. H. Johnson, 1996 b: Heating, moistening, and rainfall over the western Pacific warm pool during TOGA COARE. *J. Atmos. Sci.*, **53**, 3367-3383.

Lin, Y. J., T. C., Wang, and J. H. Lin, 1986: pressure and temperature perturbations within a squall line thunderstorm derived from SESAME dual-Doppler data. *J. Atmos. Sci.*, **43**, 2302-2327.

Lilly, D.K., 1979: The dynamic structure and evolution of thunderstorms and squall lines. *Ann. Rev. Earth planet. Sci.*, **7**, 117-171.

Lindstrom, S. S. and Nordeng, T. E., 1992: Parameterized slantwise convection in a numerical model. *Mon. Wea. Rev.*, **120**, 742-756.

Ludlam, F. H.,1963: Severe local storms: a review. *Meteor. Monogr.*, **5**, Amer. Meteor. Soc. 1-30.

-------------, 1980: *Clouds and Storms*. Pennsylvania State University Press, 404p.

Moncrieff, M. W., and J. S. A. Green, 1972: The propagation and transfer properties of steady convective overturning in shear. *Quart. J. Roy. Meteor. Soc.*, **98**, 336-352.

-------------------, 1992: organized convective systems: Archetypal dynamical models, mass and momentum flux theory, and parameterization. *Quart. J. Roy. Meteor. Soc.*, **107**,29-50.

Morse, P. M., and H. Feshbach, 1953: *Methods of Theoretical Physics*. Part **II**, 1092-1106.

Newton, C.W., 1966: Circulations in large sheared cumulonimbus. *Tellus*, **18**, 699-713.

Nordeng, T. E., 1987: The effects of vertical and slantwise convection on the simulation of polar lows. *Tellus*, **39A**, 354-375.

Nuss, W. A., and D. W. Titley, David W., 1994: Use of multiquadratic interpolation for meteorological objective analysis. *Mon. Wea. Rev*, **122**, 1611-1631.

Ogura, Y., and N. A. Phillips, 1962: A scale analysis of deep and shallow convection in the atmosphere. *J. Atmos. Sci.*, **30**, 1276-1286.

Pan, D.-M., and D. A. Randall, 1998: A cumulus parameterization with a prognostic closure. *Quart. J. Roy. Meteor. Soc.*, **124**,949-981.

Parker, D. P., and R. H. Johnson, 2000: Organizational modes of midlatitude mesoscale convective systems. *Mon. Wea. Rev.*, **128**, 3413-3436.

Petersen, W.A., R.C. Cifelli, S. A. Rutledge, B.S. Ferrier and B.F. Smull, 1999: Shipborne dual-Doppler operations during TOGA COARE. Integrated observations of storm kinematics and electrification. *Bull. Amer. Meteorol. Soc.*, **80**, 81-97.

Randall, D. A., K.-M. Xu, R. J. C. Somerville, and S. Iacobellis, 1996: Single-column models and cloud ensemble models as links between observations and climate models. *J. Climate*, **9**, 1683-1697.

Randall, D. A. and D. G. Cripe, 1999: Alternative methods for specification of observed forcing in single-column models and cloud system models, *J. Geophys*, **104**, 24,527-24,545.

Redelsperger, J. L., P. R. A. Brown, F. Guichard, C. Hoff, M. Kawasima, S. Lang, T. Montmerle, K. Saito, C. Seman, W. K. Tao and L. Donner, 2000: A GCSS model intercomparison for a tropical squall line observed during TOGA-COARE. Part I: Cloud-resolving models. *Quart. J. Roy. Meteor. Soc.*, **126**, 823-863,

Robe, F. R. and K. A. Emanuel, 2001: The effect of vertical wind-shear on radiative-convective equilibrium states. *J. Atmos. Sci.*, **58**, 1427-1445.

Rotunno, R., and J. B. Klemp,1982: The influence of the shear-induced pressure on the thunderstorm motion. *Mon. Wea. Rev.*, **110**,136-151.

---------------,------------------, and M. L. Weisman, 1988: A theory for strong, long-lived squall lines. *J. Atmos. Sci.*, **45**,463-485

Schneider, E. K., and R. S. Lindzen, 1976: A discussion of the parameterization of momentum exchange by cumulus convection. *J. Geophys. Res.*, **81**,3158-3160.

Seitter, K. L., and H. L. Kuo,1983: The dynamical structure of squall-line type thunderstorms. *J. Atmos. Sci.*, **40**, 2832-2854.

Shapiro, L. J., and D. E. Stevens, 1980: Parameterization Of convective effects on the momentum and vorticity budgets of synoptic-scale Atlantic tropical waves. *Mon. Wea. Rev.*, **108,** 1816-1826.

Simpson, J., and V. Wiggert, 1969: Models of precipitating cumulus towers. *Mon. Wea. Rev.*, **97**, 471-489.

Soong, S.-T., and W.-K. Tao, 1984: A numerical study of the vertical transport of momentum in a tropical rain band. *J. Atmos. Sci.*, **41**, 1049-1061.

Stevens, D. E., 1979: Vorticity, momentum and divergence budgets of synoptic-scale wave disturbances in the tropical eastern Atlantic. *Mon. Wea. Rev.*, **107**, 535-550.

Stokes, G. M., and S. E., Schwartz, 1994: The Atmospheric Radiation Measurement (ARM) program: Programmatic background and design of the cloud and radiation test bed. *Bull. Amer. Meteor. Soc.*, **75**, 1201-1221.

Suarez, M., A. Arakawa, and D. A. Randal, 1983: Parameterization of the planetary boundary layer in the UCLA General Circulation Model: Formulation and results. *Mon. Wea. Rev.*, **111**, 2224-2243.

Sui, C.-H., and M., Yanai, 1986: Cumulus ensemble effects on the large-scale vorticity and momentum fields of GATE. Part 1: Observational evidence. *J. Atmos. Sci.*, **43**,1618-1642.

--------, and M.-D. Cheng, X. Wu, and M. Yanai, 1989: Cumulus ensemble effects on the large-scale vorticity and momentum fields of GATE. Part II: Parameterization. *J. Atmos. Sci.*, **46**, 1609-1629.

Tao, W.-K., and S.-T. Soong, 1986: A study of the response of deep tropical clouds to mesoscale processes: Three-dimensional numerical experiments. *J. Annos. Sci.*, **43**, 2653-2676.

Tollerud, E. I., and S. K. Esbensen, 1983: An observational study of the upper-tropospheric vorticity fields in GATE cloud clusters, *Mon. Wea. Rev.*, **111**, 2161-2175.

Tomas, R. A. and P. J., Webster, 1997: The role of inertial instability in determining the location and strength of near-equatorial convection. *Quart. J. Roy. Meteor. Soc.*, **123**, 1445-1482.

Thorpe, A.J., M.J. Miller and M.W. Moncrieff, 1982: Two-dimensional convection in non-constant shear: a model of midlatitude squall lines. *Quart. J. Roy. Meteor. Soc.*, **108**, 739-762.

Tung, W.-W., and M. Yanai, 2001: Convective momentum transport observed during the TOGA COARE IOP. Part I: General features. In preparation for *J Atmos. Sci.*

Weisman, M. L., and J., B., Klemp, 1982: The dependence of numerically simulated convective storms on vertical wind-shear and buoyancy. *Mon. Wea. Rev.*, **110**, 504-520.

--, 1984: The structure and classification of numerically simulated convective storms in directionally varying wind-shears. *Mon. Wea. Rev.*, **112**, 2479-2498.

--, and R. Rotunno, 1988: Structure and evolution of numerically simulated squall lines. *J Atmos. Sci.*, **45**,1990-2013.

Wu X., and M., Yanai, 1994: Effects of vertical wind-shear on the cumulus transport of momentum: observations and parameterization. *J. Atmos. Sci.*, **51**, 1640-1660.

Yau, M. K., 1979: Perturbation pressure and cumulus convection. *J. Atmos. Sci.*, **36**, 690-694.

Zhang, G. J., and H.-R. Cho, 1991a: Parameterization of the vertical transport of momentum by cumulus clouds. Part I: Theory. *J. Atmos. Sci.*, **48**, 1483-1492.

--------------, and--------------, 1991b: Parameterization of the vertical transport of momentum by cumulus clouds. Part II: Application. *J. Atmos. Sci.*, 48, 2448-2457.

--------------, and N. A. McFarlane, 1995: Role of convective scale momentum transport in climate simulation. *J. Geophys. Res.*, 100, 1417-1426.